Tyre dynamics, tyre as a vehicle component
Part 1.: Tyre handling performance

Virtual Education in Rubber Technology (VERT), FI-04-B-F-PP-160531
Joop P. Pauwelussen, Wouter Dalhuijsen, Menno Merts
HAN University
October 16, 2007

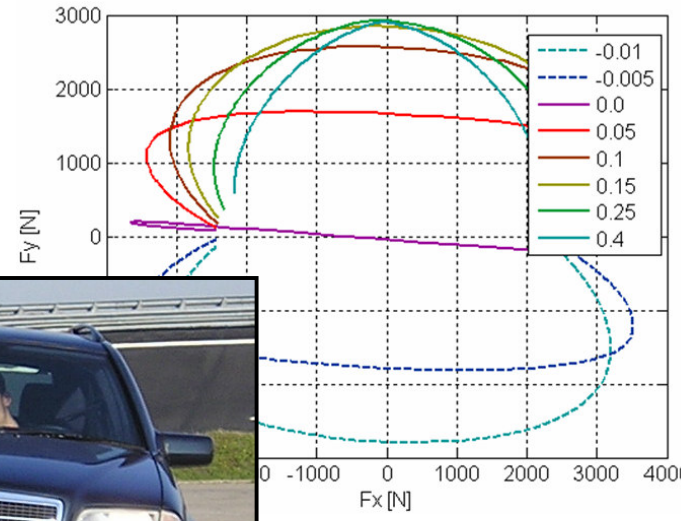

Table of contents

1. General

The vehicle handling performance is directly related to the tyre-road contact.
The tyres transfer the horizontal and vertical forces acting on the vehicle as a result of steering, braking and driving in combination with possible road disturbances or external disturbances like aerodynamic forces due to for example cross-wind.

The relationship between vehicle behavour and these tyre-road contact forces depends on the specific tyre design, tyre condition variables like slip and tyre load, the road

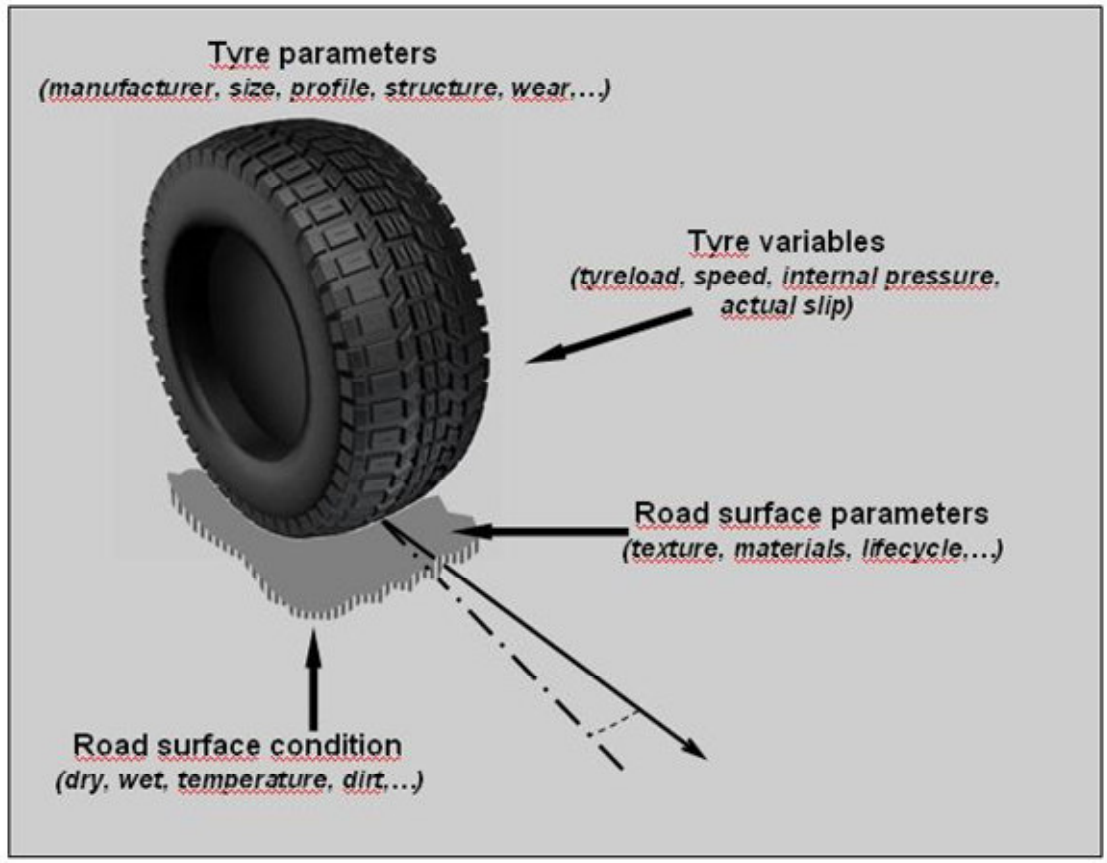

Figure 1.: The tyre-road interface

surface design, and the actual road surface and weather conditions, see figure 1. Tyre design parameters are related to the tyre geometry (width, sidewall height,...), the specific tyre brand (manufacturer), the tread pattern design, the structure of the tyre (a tyre is built up from different rubber compounds and rubberized fabric or cord acting as reinforcement elements, referred to as plies), the amount of wear, etc.
More wear may result in a higher stiffness and therefore higher contact forces for the same slip, with slip referring to the deviation of the tyre condition from free rolling conditions (explained more rigorously in the next sections).

1.1. Effect of tyre ply-design

One may be familiar with the different performance of bias-ply tyres and radial-ply tyres, being a direct result of the different ply-designs of the two tyre types, see figure 2.

For a bias-ply tyre, the belt plies cross over at each other at a large angle (in the order

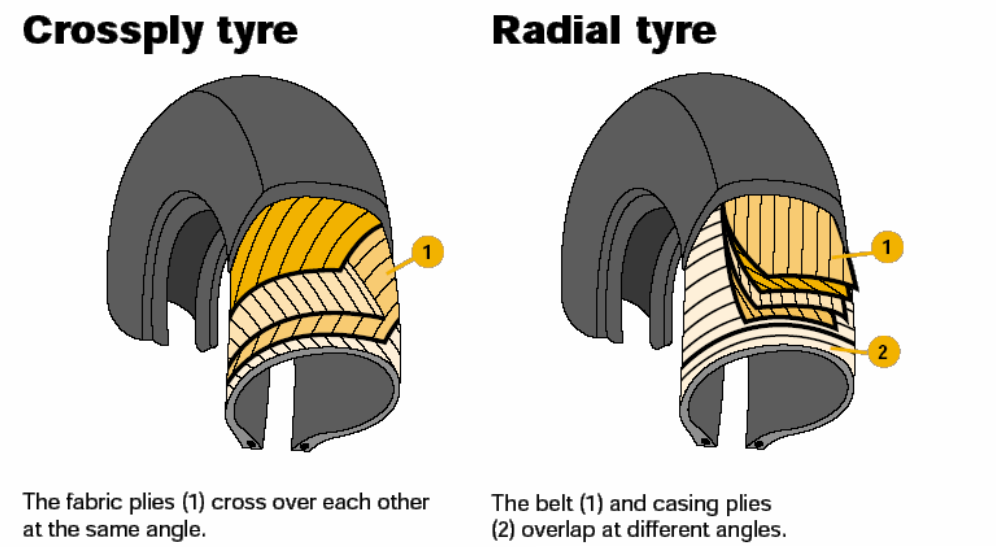

Figure 2.: Structure of bias-ply and radial-ply tyre, from [34]

of 40° with respect to the circumferential direction), and are extended over the sidewalls, in contrast to the radial-ply tires with distinction between belt plies (with orientation being close to circumferential) and radial casing plies. Due to these structural differences, the tread motion is reduced for the radial-ply tyre, and the cornering stiffness ('stiffness against cornering', treated in detail later in this chapter) is usually exceeding that for the bias-ply tyre. In figure 3, shear stresses in the contact area along the tyre width are shown, indicating stress concentrations at the tyre shoulders for bias-ply tyres, due to interaction of tread motion and side wall deformation. This contributes to more wear. In addition, bias-ply tyres experience more dissipation, having a positive effect on ride.

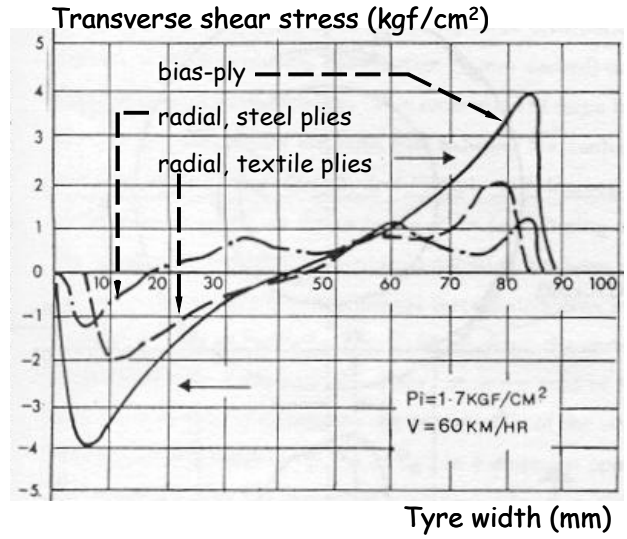

Figure 3.: Transverse shear stress for bias-ply and radial-ply tyres, from [20]

1.2. Tyre variables and tyre performance

Tyre load is related to vehicle mass and axle load distribution, and therefore also to loading conditions. Under specific braking, driving or cornering conditions, roll and pitch will occur and tyre loads will change, leading to different response of the tyre-road contact in terms of tyre forces. There is a dependency of tyre-road contact performance on vehicle and tyre forward velocity. Changing the internal tyre pressures will result in a modified contact area and consequently modified local normal pressures in the contact area. This will affect the local shear stress behaviour, building up the horizontal contact forces.

1.3. Road surface parameters

One may distinguish different road surface design in terms of micro- and macrotexture describing the local roughness and adhesion potential, the used materials (asphalt, concrete,..), and the composition of the materials (dense asphalt, drain asphalt,..).
In figure 4, we show some of the effects of the road surface texture on the vehicle and tyre performance (from [33]).

The handling characteristics, i.e. the topic of this chapter, is affected by road texture for wavelengths between values far less then 1 mm, and in the order of 0.5 until 1 meter. Tyre wear is typically a phenomenon related to wavelengths less then 1 cm. Internal vehicle noise is arising from large wavelengths (of course also depending on vehicle speed). Rolling resistance, discomfort and vehicle wear are most affected by the more coarse parts of the road texture as well, and even (discomfort, vehicle wear) by the more global vehicle unevenesses.

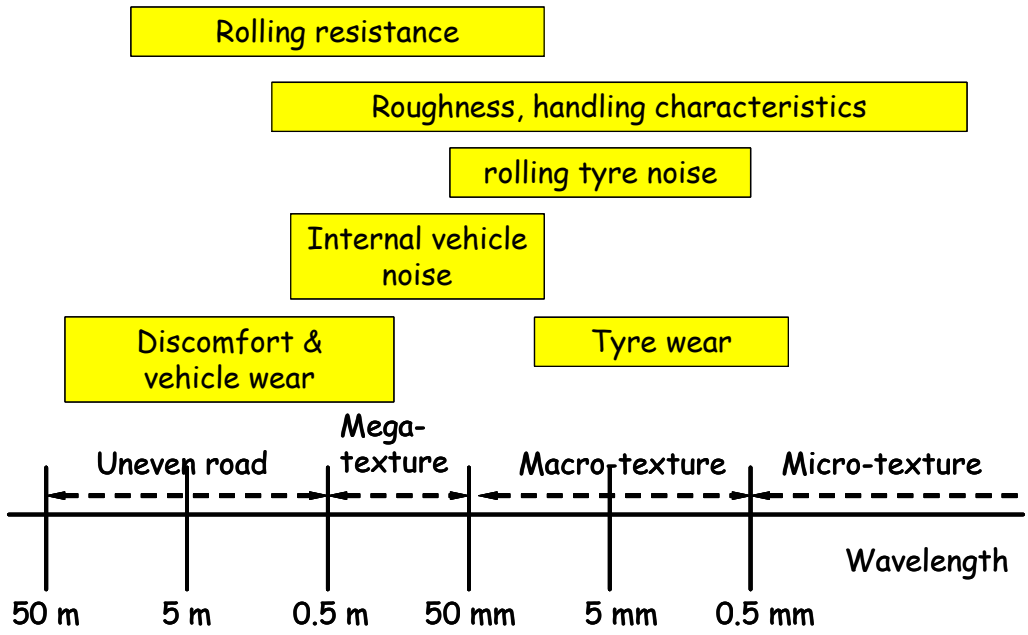

Figure 2.: Functional properties road surface vs. texture wave length

Road conditions vary in time due to ageing. Due to road use, there will be road surface wear and polishing effects, leading to different friction under similar weather conditions. Finally, the weather conditions itself obviously have a strong effect on the tyre-road conditions, where one may think of rain, snow, variation of temperature, and the impact of rain mixing up with dirt after a long dry period leading to significant reduction in road friction.

1.4. Tyre input and output quantities.

A tyre is schematically shown in figure 5, with indication of al the input and output quantities, see also [18]. There are three forces and three moments acting on the tyre:

F_x : braking, driving force
F_y : lateral (cornering) force
F_z : tyre load, to carry the vehicle weight
M_x : Overturning moment
M_y : Moment about the wheel axis (driving, braking torque)
M_z : Self-aligning moment

Most of these forces and moment will be explained later in more detail.
A tyre travels with a horizontal velocity V, with components V_x and V_y in longitudinal and lateral direction. Due to brake or drive torque and cornering forces, slip will occur which means that the tyre slides with nonzero speed over the surface. The corresponding slip speeds V_{sx} and V_{sy} are shown in figure 5 as well. The tyre rolls over the surface with an angular speed Ω, leading to the so-called rolling speed:

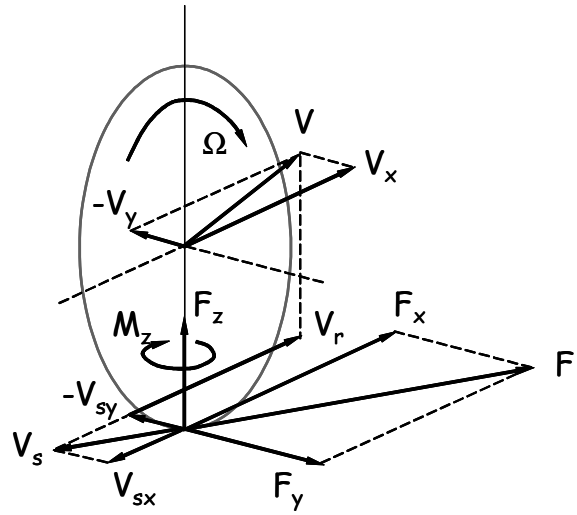

Figure 3.: Input and output quantities acting in a tyre

$$V_r = \Omega . R_e$$

with R_e being the **effective rolling radius** of the tyre under free rolling. For a free rolling wheel, the rolling speed coincides with V_x, defining the effective rolling radius as the ratio between V_x and Ω.

1.4.1.: The effective rolling radius

The effective rolling radius is not the same as the **loaded tyre radius** R_l, with the latter being defined as the vertical distance between the wheel centre and the horizontal surface. A free rolling tyre rotates around a point near the contact patch. For a rigid wheel on a flat horizontal surface, this point coincides with the single contact point between tyre and road, and the forward speed V_x equals angular speed time (loaded = unloaded) radius.

For a pneumatic tyre, the distance between points at the circumference of the tyre and the wheel centre varies from a value close to the unloaded radius just before entering the contact area to the same value as the loaded radius just at the projection point of the wheel centre on the contact area. At that point, the peripheral velocity of the tread (relative to the wheel centre) coincides with the horizontal velocity V of the wheel centre. Moving out of the contact area, the tread regains its original length and the peripheral velocity returns to Ω.R with R the unloaded radius. As a consequence, the spin speed of the wheel with a pneumatic tyre under conditions of free rolling is less than that of a rigid wheel and:

$$R_l < R_e < R$$

It means that the centre of rotation of the wheel usually lies somewhere below the surface. The effective rolling tyre under free rolling also behaves different with varying tyre load compared to the loaded tyre radius. A loaded radius behaves almost linear in the tyre load F_z, i.e. the tyre behaves as a linear spring in vertical direction. The effective rolling radius varies significantly with tyre load. This can be described based on empirical fit as follows (see [1]:

$$R_{e,free\_rolling} = R - \rho_0.[D.\arctan(B.\frac{\rho}{\rho_0}) + E.\frac{\rho}{\rho_0}]$$

with tyre deflection ρ, tyre deflection ρ_0 for nominal tyre load F_{zo}, and fitparameters B, D, E which may vary according to:

3 < B < 12	: B stretches the effective tyre characteristic curve along the F_z -axis (ordinate). B large means a large slope at $F_z = 0$.
0.2 < D < 0.4	: shift from asymptote at high wheel loads
0.03 < E < 0.25	: with low values of E for stiff tyres

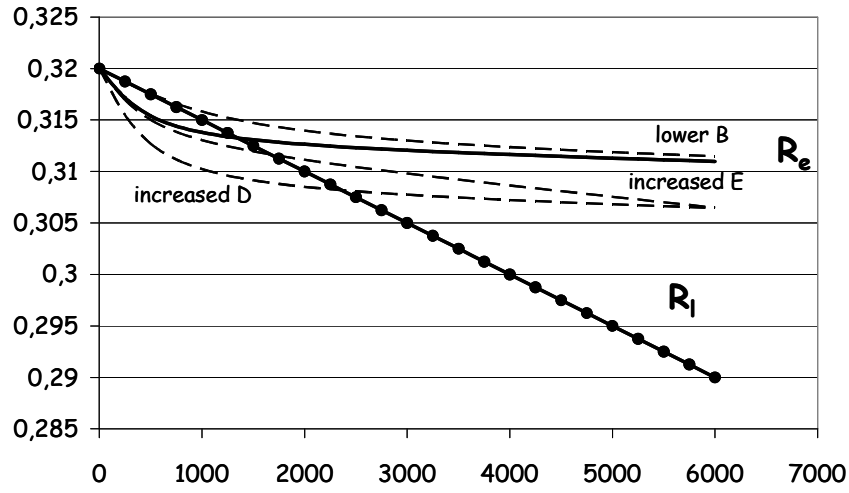

Figure 4.: Effective and loaded tyre radius under conditions of free rolling

An example of the variation of R_l and R_e is shown in figure 6 for B = 10, D = 0.25 and E = 0.05. The tyre stiffness is taken as 2.10^5 N/m. The unloaded radius R is taken as 0.32 m and we choose F_{z0} = 4000 N. We have also varied the parameters to illustrate the range of possible effective rolling radius characteristics.

The effective rolling radius turns out to increase with increasing speed and increasing inflation pressure. The variation with speed is strongly dependent on the tyre carcass structure.

.

A radial-ply tyre rolling radius appears to be almost constant for varying speed in contrast with the diagonal-ply (bias-ply) tyre. This phenomenon has to do with the radial response of the tyre to higher circumferential speeds.

2. The rolling tyre.

Let us discuss the rolling tyre in more detail, see figure 7 (see also [20]). With the tread entering and moving through the contact area, the distance to the wheel centre changes from the unloaded radius to the loaded radius and back to the unloaded radius. With the peripheral speed in the contact area corresponding to the effective rolling radius in between these values, points in the contact area need to catch up with this peripheral speed at the both ends of the contact area where the distance of contact points to the wheel centre exceeds R_e. As a consequence, one observes rearward slip at these parts. With a similar argument, the points of the tyre circumference are slowed down in speed in the centre part of the contact area, corresponding to forward slip. Integration of the slip over contact area results in the global performance related to the shear stress as indicated in figure 7. The peripheral speed with respect to the wheel centre is shown in the lowest graph in figure 7, reducing from the unloaded speed Ω.R just before the contact area to the speed $\Omega.R_e$ within the contact area.

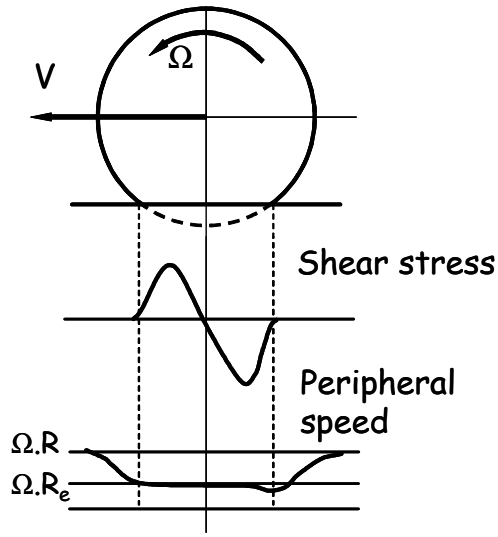

Figure 5.: Free rolling tyre

The total longitudinal net force, determined from integrating the shear stress over the contact area will be a nonzero, negative force, known as the **rolling resistance force**. This rolling resistance force corresponds to a moment acting around the wheel centre, being balanced by the moment resulting from the tyre load. Consequently, the net tyre load will have to act along a force line, slightly in front of the wheel centre.

3. The tyre under braking or driving conditions.

Now consider a tyre under a braking torque, as indicated in figure 8.
The brake torque M_y has to be balanced by moments due to a brake force $-F_x$ and the tyre load F_z.
The offset of the tyre load in front of the wheel centre increases with respect to the free rolling tyre. The tyre will experience a slip speed of wheel w.r.t. ground, reducing the angular speed and therefore increasing the effective rolling radius R_e. If M_y is large enough, $R_{e,braking}$ will exceed the loaded radius .
The total longitudinal shear stress in the contact area now consists of a part due to free rolling (dashed in figure 8) and a superimposed shear stress caused by braking. As a results, the major part of the tyre in the contact area is stretched due to the braking torque. Tread elements entering the contact area first try to adhere to the road surface, with the longitudinal deflection and therefore the shear stress increasing linearly along the contact zone. At a certain point, the shear stress reaches the limits of friction ($\mu.\sigma_z$ with local road friction μ and normal stress σ_z under Coulomb law) and the treads start to slide. As a result, the shear stress drops down along the rear part of the contact zone. In a similar way as discussed for a free rolling tyre, one arrives at a distribution of the peripheral velocity of treads (w.r.t. the wheel center) as shown in the bottom part of figure 8.

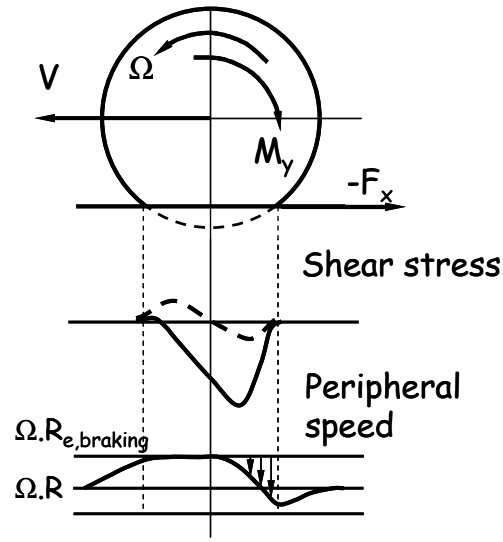

Figure 8.: Braking rolling tyre

Note that, in general, sliding starts at the rear of the contact ares and extends towards the front part of the contact area for increasing brake torque, until finally sliding is apparent along the full contact area.

In case of a tyre under driving conditions, the angular speed is increased and therefore the effective rolling radius $R_{e,driving}$ decreased. The drive torque has to balance moments resulting from a driving force in the contact area and the tyre load. The offset of the tyre load line in front of the wheel centre is decreased with respect to the case of the free rolling tyre. The shear stress is now built up from the free rolling distribution plus a triangular shaped pattern along the contact area, and the tyre tread material is experiencing a compression.

3.1. Practical brakeslip

We introduce the practical longitudinal brakeslip κ as follows:

$$s_x \equiv -\kappa = \frac{V_{sx}}{V_x} = \frac{V_x - \Omega.R_e}{V_x} \equiv -\frac{\Omega - \Omega_0}{\Omega_0}$$

with slip speed V_{sx} of tread elements with respect to the road surface (obtained from the difference of the forward tyre speed V_x at the wheel centre with respect to the road surface, and the peripheral speed $\Omega.R_e$ of tread elements with respect to the wheel centre), and the angular speed Ω_0 under free rolling conditions. Observe that, under braking, κ varies between -1 (locked wheel, $\Omega = 0$) and 0 ($V_{sx} = 0$).

When a driver starts braking, the angular speed per wheel is changed, where the rotational wheel inertia I_{wheel} is decelerated by the resultant of the brake torque and the tyre brake force:

$$I_{wheel}.\dot{\Omega} = -M_y - R_l.F_x(\kappa)$$

with $F_x > 0$ in positive x-direction (i.e. $F_x < 0$ in case of braking). This equation is part of a larger set of equations to solve the braking problem for a vehicle. Clearly, the forward vehicle speed (being included in the above angular wheel velocity equation through the slip κ) will decrease. The resulting forward vehicle speed follows from another equation describing the balance of the vehicle inertia deceleration and the wheel forces:

$$m_{vehicle}.\dot{V}_x = \sum_{all\,wheels} F_x(\kappa)$$

3.2. Longitudinal slip characteristics.

In order to solve the angular wheel velocity equations for each wheel (with possibly all different slip values), one requires a description of F_x in terms of practical slip κ. A

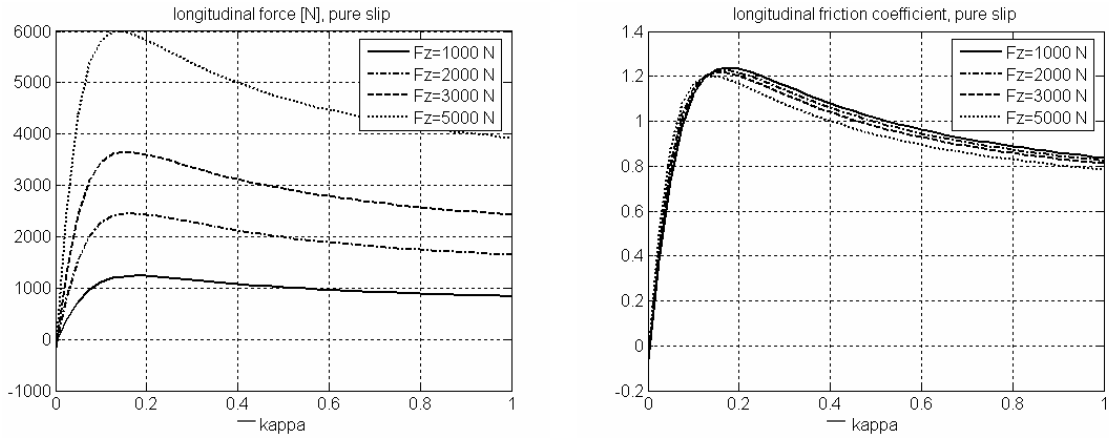

Figure 9: Brake force vs. longitudinal slip

typical behaviour of this longitudinal characteristic tyre behaviour is shown in figure 9. In the left-hand picture, we have plotted $-F_x$ (with brake force F_x) versus $|\kappa|$ whereas in the right-hand picture, we have plotted $-\mu_x \equiv -F_x/F_z$, the so-called normalized tyre force

(also known as the longitudinal force coefficient), for various values of the tyre load. Usually, the curves will not exactly pass the origin (due to rolling resistance, inaccuracies in the tyre). Clearly, the longitudinal tyre force is close to being proportional to the tyre load but not quite. The longitudinal slip stiffness, being the slope of the curve for F_x at $\kappa = 0$, tends to decrease more then proportional with F_z for increasing tyre load. One observes a peak value and a saturation value in both pictures, for the longitudinal force coefficient indicated as - μ_{xp} (peak value) and - μ_{xs} (the limit of - μ_x for pure sliding, i.e. at $\kappa = -1$). The peak value is obtained for brakeslip around 0.1 and 0.15 in absolute value (10 – 15 % slip). For small brakeslip, this characteristic can be approximated by a linear relationship, with slope being the longitudinal slip stiffness.
The peak value is the optimal value to brake, but just beyond the slip corresponding to this optimal value, the wheel will lock in very short time. That is the reason why nowadays almost all vehicles are equipped with anti-lock systems, in order to prevent to excessive brake slip. In the same way, one may discuss driveslip, and the risk of spinning of the wheel in case of too high traction. This phenomenon can be prevented using traction control systems.

3.3. Road conditions and brakeslip.

The normalized tyre force - μ_x and (therefore also the longitudinal tyre force itself) depends essentially on the tyre-road conditions, that means on things like:

- road roughness. Pavement exhibits three types of roughness, micro-texture (with wavelength less than 0.5 mm), macro-texture (wavelength between 0.5 mm and 50 mm) and mega-texture (wavelength exceeding 50 mm), see [33]
- tyre tread wear
- wet conditions (wet, possible hydroplaning, snow, ice,…)

Micro- and macro-texture are schematically shown in figure 10. Macro-texture is related to the overall roughness of the road resulting from the number, type and size of stone chippings, whereas micro texture has to do with the roughness of the individual chippings. Idealized texture leads to sufficient drainage and significant hysteretic friction (local pressures) at the cost of tyre wear. Tips should preferable be sharp to have good friction even under wet conditions, but that leads to abrasive wear. The existence of micro-texture is due to the typical asphalt ingredients (silica, sand, quartzites).

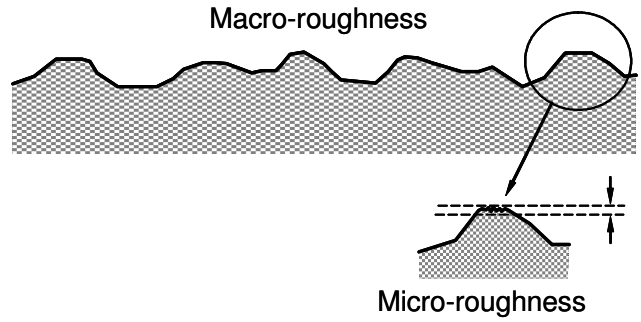

Figure 10.: Micro- and macro road roughness

Macro-texture and micro-texture vary in time. It is known from drain asphalt that, due to the situation of many small contact zones between rubber and ground, there is more

polishing effect and therefore rounded asperities, with impact on the adhesive properties of the tyre road contact. Roughly speaking one might say that macro-texture is related to a strong velocity dependence of the tyre-road contact under wet/rain conditions, whereas micro-texture is related to the slightly wet or dry-adhesive aspects. See also [17].

3.3.1. Wet road conditions.

Under wet road conditions, the longitudinal force coefficient maximum level drops, to levels in the order of 0.6 - 0.8 for a wet road, to 0.4 – 0.5 for snow, and to levels of 0.2 – 0.4 for ice.

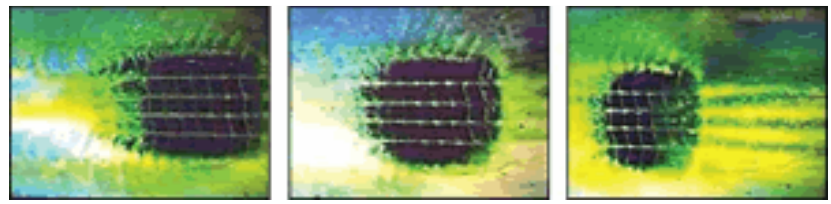

Figure 11.: Contact area on a wet road for different speeds

A special case is given when water is present on the road. In order to maintain contact between tyre and road, the water has to be evacuated, and this property may be improved by adjusting the tread block pattern of the tyre (longitudinal grooves, or

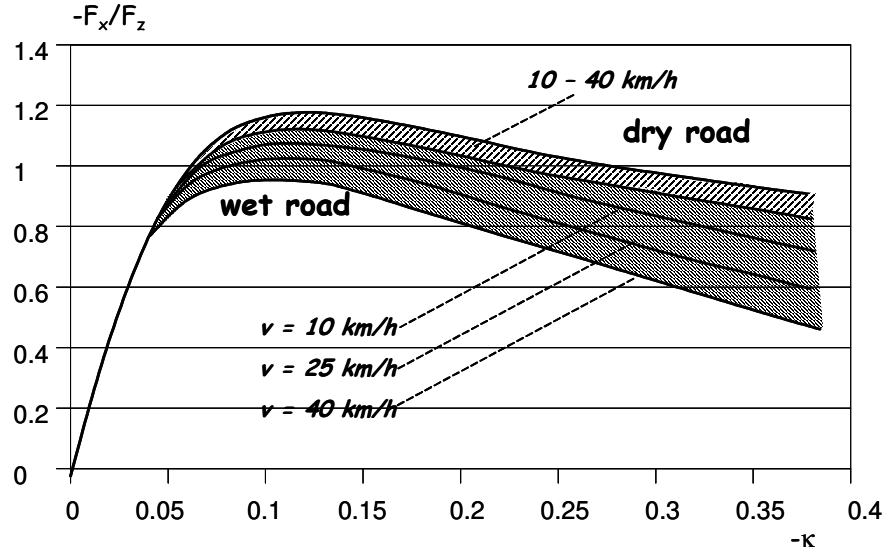

Figure 12.: The effect of road conditons and speed in the longitudinal force coefficient

grooves curved in an outward direction guiding the water in a radial direction away from the tyre). With increasing speed, there is less time to remove the water and the contact zone is further reduced, see figure 11 for an example [4] for three different speeds.

At a certain speed, the tyre may float entirely on a film of water (**hydroplaning**), and the friction coefficient drops to very low values (< 0.1). In other words, hydroplaning

occurs when a tyres is lifted from the road by a layer of water being trapped in front of and under a tire.
One usually distinguishes between **dynamic hydroplaning** (water is not removed fast enough to prevent loss of contact) and **viscous aquaplaning** when the road is contaminated with dirt, oil, grease, rubber-parts, leaves etc. Usually, regular rain will wash this away, but especially after a long dry period with dirt, dust etc. having piled up, a sudden rain may result in a more viscous mixture on the road causing unexpected dangerous (i.e. low friction) conditions.
In figure 12, the qualitative effect of road conditions and velocity on the longitudinal force coefficient is shown. These graphs agree with results, presented in [10]. One observes a minimal effect of velocity in case of a dry road in contrast to the situation when the road is wet. In the latter case, the brake force drops significantly with vehicle velocity.

3.3.2.: Road conditions, wear, tyre load and speed

The impact of aquaplaning in combination with wear is illustrated in figure 13, taken from [10], with the locked wheel longitudinal force coefficient value plotted against vehicle velocity. As expected, this locked wheel value is further reduced under tread wear conditions. The hydroplaning velocity is reduced with increasing water layer depth. Similar results for the peak wheel longitudinal force coefficient are shown in figure 14 (from [14]).

The combined effect of speed, road condition and tyre load is shown in figure 15, in terms of the peak longitudinal coefficient μ_{xp} and the sliding longitudinal coefficient μ_{xs}, from [5].

Sliding coefficients are more sensitive to speed than the peak values. The sensitivity of speed on the peak value increases if the road gets wet.

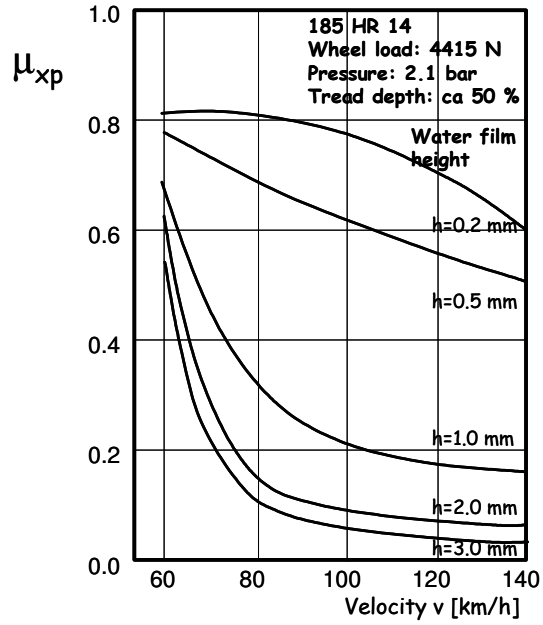

Figure 14.: Maximum friction coefficient for different water film heights and vehicle speeds [14]

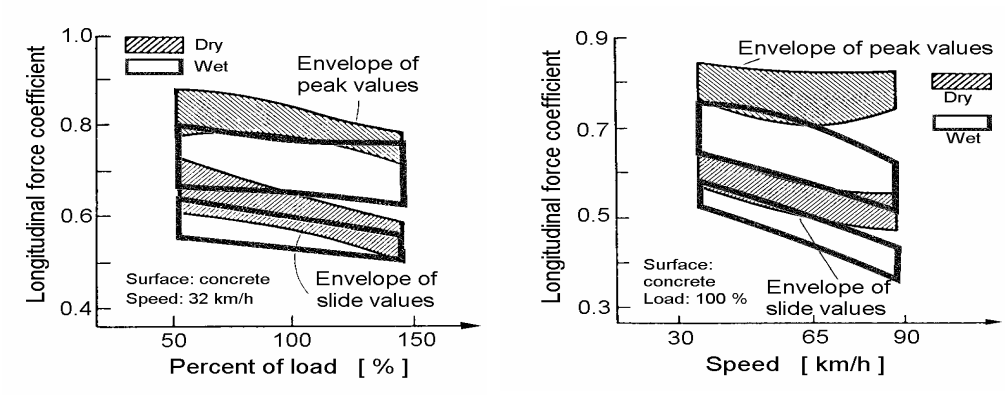

Figure 15.: Combined effect of speed, tyre load and road condition on peak and sliding longitudinal coefficient, from [5]

3.4. Tyre models for longitudinal slip behaviour

There are different ways to describe the longitudinal slip behaviour using tyre models. One distinguishes between **physical models** and **empirical models**. A physical model describes the tyre on the basis of the recognized physical phenomena during braking, usually in a simplified way. Such simplified models do not aim to give a quantitative description of the tyre handling performance, but merely give an explanation of the qualitative phenomena (shape of the curve, trends in the sense that the impact of changing vehicle speed, road conditions etc. are well covered, etc.). These models can be used for longitudinal behaviour, cornering behaviour and combined slip behaviour, and will therefore be addressed in section 5.
More complex physical models are for example Finite Element models, applied in order to derive quantitatively correct tyre performance based on a detailed description of the tyre structure and material properties. That means that FE models form a link between tyre design and tyre performance. However, FE-models are very time consuming, both in CPU-time and in preparation time (setting up the model).

Empirical tyre models are based on a similarity approach where experimental results are used to find parameters to tune a certain mathematical description. A well-know empirical tyre model is de Magic Formula model, due to H.B. Pacejka, therefore also often referred to as the Pacejka model. This Pacejka model has been implemented in many different versions. We refer here to the version being implemented in ADAMS/tyre, originated from DELFT-TYRE, see [22] and [1]. We note here that, different from the preceding analysis, the Pacejka tyre model assumes a z-axis pointing upward. i.e. with the y-direction pointing port side.

3.5. The pure slip longitudinal Magic Formula description

The basic mathematical formula describing the longitudinal characteristics is given by the so-called sine-version, given by:

$$Y(x) = F_x(x) = D.\sin(C.\arctan(B.x - E.(B.x - \arctan(B.x)))) + S_V$$

with Y(x) being either F_x or F_y, and x - S_H being either the longitudinal slip κ or the lateral slip tan (α) for slip angle α (see next section). The parameters S_H and S_V are so-called shifts to allow the curve not to pass through the origin (i.e. Y(x) = 0 does not automatically imply x = 0).
D is related to the peak of the longitudinal force coefficient and the wheel load:

$$D = \mu_{xp}.F_z$$

Neglecting camber, the Magic Formula give for μ_{xp}:

$$\mu_{xp} = (p_{xD1} + p_{xD2}.df_z) \text{ with } df_z = \frac{F_z - F_{z0}}{F_{z0}}$$

with **nominal tyre load** F_{z0}.
The nominal tyre load is related to the maximum admissible static load for the specific temperature and speed index, usually referred to as the **ETRTO value** (European Tyre and Rim Technical Organisation). The speed index indicates the maximum speed for which the tyre is allowed to be used, before it destroys itself due to overheating, as a result of high-frequency standing waves responsible for a strong increase of internal deformation power being converted into heat
Choosing the nominal value F_{z0} being equal to 80 % of this ETRTO value, a reasonable choice for F_{z0} is listed in table 1.

Class	***F_{z0} [N]***	***Example***
Compactclass	3000	VW-Polo
Middle class	5000	VW-Passat, BMW-5,..
Topclass	6000	Audi A8

Table 1.: Some typical values for the nominal tyre load F_{z0}.

Hence, a specific nominal tyre load is related to a class of tyres, with the same maximum allowable operating speed. Different nominal tyre loads refer therefore to different classes of tyres, in contrast to the variation in tyre load for one specific tyre (due to static load variations, load transfer during cornering, etc.).

Other parameters in the Pacejka tyre formula for pure longitudinal slip can be expressed as follows (neglecting camber):

$$BCD = F_z.(p_{Kx1} + p_{Kx2}.df_z).\exp(p_{Kx3}.df_z)$$

$$E = (p_{Ex1} + p_{Ex2}.df_z + p_{Ex3}.df_z^2).(1 - p_{Ex4}.sign(\kappa))$$

$$S_H = (p_{Hx1} + p_{Hx2}.df_z)$$

$$S_V = F_z.(p_{Kx1} + p_{Kx2}.df_z)$$

A typical value for C = C_x is given by C_x = 1.68. For further suggestions for parameters, we refer to [1].

4. The tyre under cornering conditions

Let us consider a tyre under cornering conditions, as indicated in figure 16. Under cornering conditions, there exists a local velocity vector, being in general not parallel to the wheel centre plane. This wheel centre plane is defined as the symmetry plane of the tyre such that forces acting in the symmetry plane do not contribute to the lateral force for the tyre.
In the front part of the contact are, the treads of the tyre try to follow this local speed direction, resulting in a displacement along the tyre circumference within the contact are, increasing linearly from zero (just in front of the contact area) up to a situation where the induced lateral shear stress just reaches the maximum possible shear stress level, i.e. $\mu.\sigma_z$ with local road friction μ and normal stress σ_z under Coulomb law. We have discussed a similar phenomena for braking and driving (traction) of the tyre. Beyond that point, the treads of the tyre will slide leading to a reduction of the shear

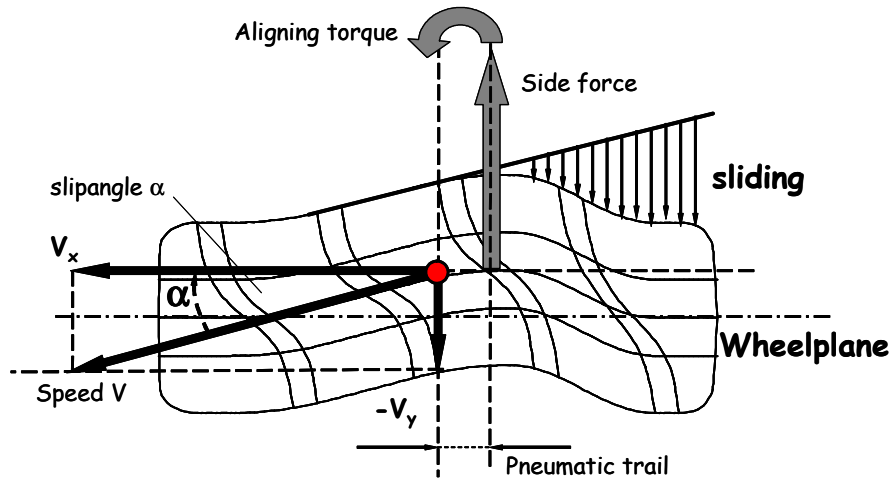

Figure 16.: Tyre under cornering conditions

stress in the direction of the contact area rear end. Clearly, when sliding and in the absence of longitudinal slip, the lateral shear stress will be equal to $\mu.\sigma_z$. With σ_z reducing to zero at the edges of the contact area, the friction limits for the shear stress will decrease further, and sliding is likely to extend until the contact area rear end.

Deflection of the tyre is due to two separate effects, (1) the deflection of the contact rubber, i.e. of the treads, and (2) deflection of the belt.
Both compliances allow the tyre to direct itself to the local speed direction, but the stiffness are different. In terms of physical models, one may distinguish here between the so-called brush model and the stressed string model. Both will be treated in more detail in section 5.

We introduce the practical lateral slip as - tan(α) , i.e.

$$s_y = -\tan(\alpha) = \frac{V_{sy}}{V_x} = \frac{V_y}{V_x}$$

with slip speed V_{sy}. As we will see later, the practical slip quantities correspond with a description of tyre deflection in terms of deformed quantities. An alternative approach might be to express slip in terms of the undeformed coordinate system. This will result in the so-called theoretical slip quantities, defined as:

$$\rho_x = \frac{V_{sx}}{V_r} \;\; ; \;\; \rho_y = \frac{V_{sy}}{V_r}$$

Using

$$\kappa = \frac{V_r - V_x}{V_x} = \frac{\Omega.R_e - V_x}{V_x}$$

one easily arrives at the following relationship between practical and theoretical slip quantities:

$$\rho_x = \frac{s_x}{1 - s_x} \;\; ; \;\; \rho_y = \frac{s_y}{1 - s_x}$$

As we observed before, the practical brake slip s_x varies between 0 and 1, whereas under driving conditions, $-\infty < s_x < 0$, i.e. the practical driveslip may attain very large absolute values in case of wheel spinning on the spot. In contrast to the practical slip, the theoretical longitudinal slip remains bounded under driving conditions but may grow to large absolute values in case of braking when the wheel gets locked.

4.1. Vehicle cornering performance

Vehicle dynamics analysis includes relationships between slip angles at front and rear axles (and possibly at the separate wheels) and global vehicle performance output variables such as yaw-rate and lateral vehicle speed (or, equivalently, the body side slip angle). See figure 17 for a schematic layout of a vehicle under cornering conditions. The four tyre forces balance the centripetal force, acting on the vehicle in local lateral direction:

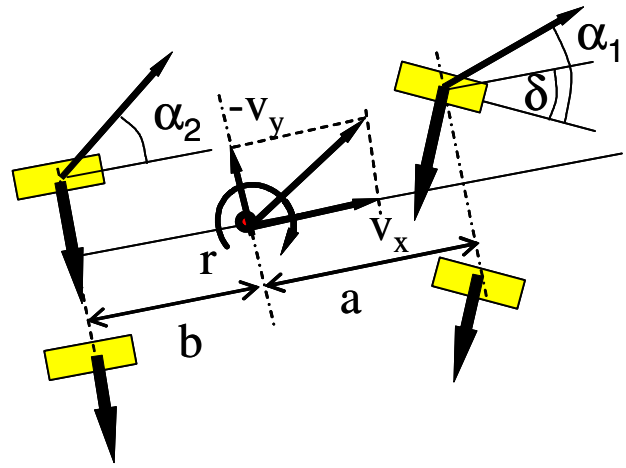

Figure 17.: Vehicle handling, schematically

$$m_{vehicle}.(\dot{v}_y + V_{vehicle}.r) = \sum_{all\_wheels} F_y(\alpha)$$

with lateral vehicle speed at the centre of gravity, v_y and yaw rate r. In addition, the moments of the four tyre around the centre of gravity have to balance the total inertial moment, approximated by:

$$I_{vehicle}.\dot{r} = \sum_{front\_wheels} a.F_y(\alpha) - \sum_{rear\_wheels} b.F_y(\alpha)$$

with vehicle moment of inertia in vertical z-direction $I_{vehicle}$. Note that, for small slip angles and steering angle, the vehicle speed can be approximated by V_x (and vice versa).

Usually, one assumes the slip angles to be identical for both front wheels, and likewise for both rear wheels. Slip angles are defined by the orientation of the local velocity vector, relative to the wheel symmetry plane. With the variables as indicated in figure 17, one easily finds for the local outward lateral velocity at the front and rear wheels:

Local speed front tyre : $-V_y - r.a$

Local speed rear tyre : $-V_y + r.b$

Hence,

$$\alpha_1 \approx \tan(\alpha_1) = \delta - \frac{V_y + r.a}{V_{vehicle}} \quad ; \; \alpha_2 \approx \tan(\alpha_2) = -\frac{V_y - r.b}{V_{vehicle}} \quad ;$$

4.2. Lateral slip characteristics

In order to solve the two equations above, one requires a description of the lateral force in terms of practical slip tan(α) ≈ (α). A typical behaviour of this lateral characteristic tyre behaviour is shown in figure 18.

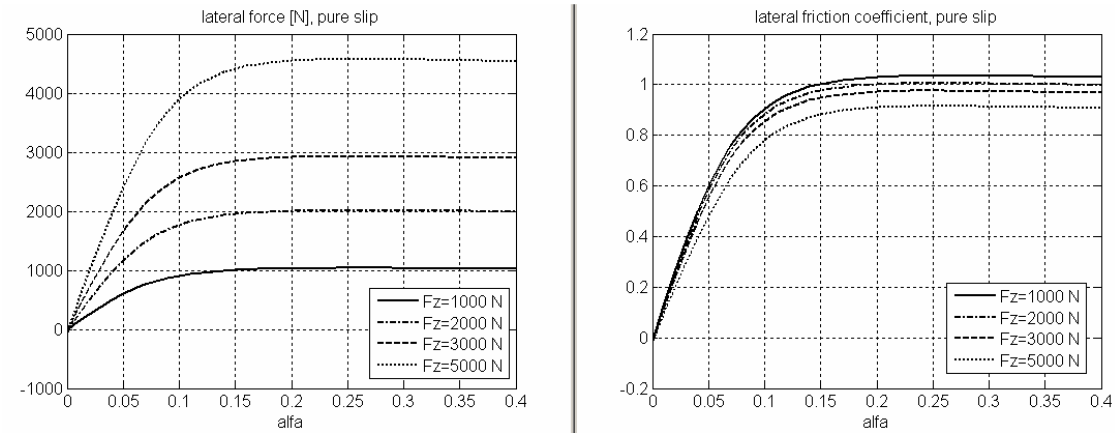

Figure 18.: Cornering force vs. slipangle, camber angle = 0

Similar as in case of braking or driving, we have plotted both F_y and $\mu_y \equiv F_y/F_z$, the so-called normalized tyre force or the **lateral force coefficient (sideforce coefficient)**, for various values of the tyre load. Again, one observes the tyre force to be close to being proportional to the tyre load but not quite.
One observes peak values and saturation values in both pictures, indicated for the lateral force coefficient as the peak value μ_{yp}, and μ_{ys} as the limit of μ_y when the tyre is drifting for large slip angle. For small slipangle, this characteristic can be approximated by a linear relationship, with slope being the **normalized lateral slip stiffness** or the normalized cornering stiffness**.**

4.3. Side force coefficient for different textures and speeds

Some values of the sliding sideforce coefficient μ_{ys} for different texture depth are shown in figure 19, under wetted conditions. One observes an increase in side friction force with texture depth (except for the Bridport surface). The Bridport surface is rather smooth (pebbles included), eliminating the adhesion coefficient of friction for wetted sliding conditions. Observe also the effect of speed, with increased speed lowering the friction, especially with small texture depth (as expected).

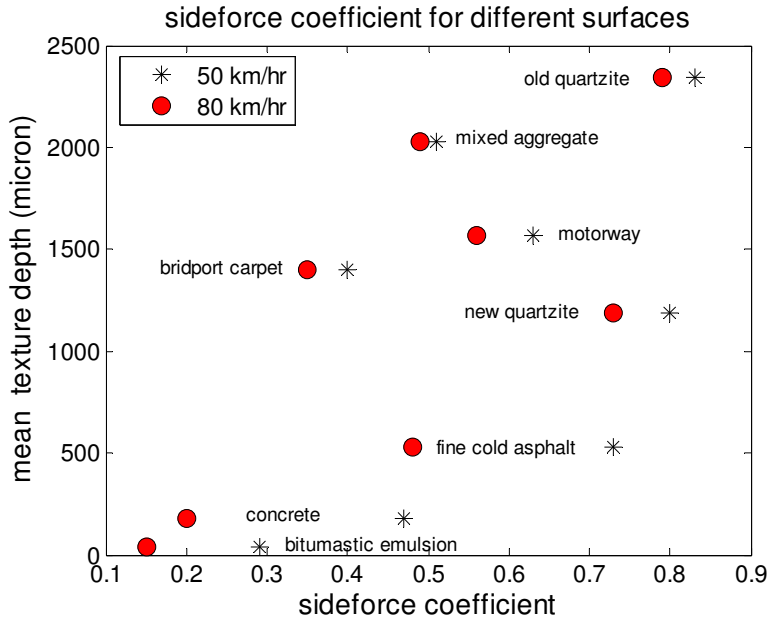

Figure 19.: Sideforce coefficient (μ_{ys}) for different texture depths and velocities

4.4. Cornering stiffness versus tyre load

The lateral slip stiffness or cornering stiffness $C_{y\alpha}$ being the slope of F_y (α) at $\alpha = 0$ (the slope in the left-hand picture in figure 18, see section 4.2), tends to decrease more then proportional with F_z for increasing tyre load.
The cornering force is shown in figure 20 vs. tyre load. This non-linear relationship is important in the sense that, during cornering, the tyre load of the outer wheel will

increase whereas the inner wheel load will decrease. Due to the nonlinear dependence of cornering stiffness on tyre load, the change in cornering stiffness at the outer wheel is exceeded in absolute value by the change at the inner wheel. For this reason, the average cornering stiffness for the full axle is decreased. With different roll stiffnesses at front and rear axle, this works out differently at both axles.
We will see later that the cornering performance of the vehicle strongly depends on the axle characteristics. As a result, this performance will change with increasing roll. Hence, by actively controlling the roll stiffness at front and/or rear axle, one is able to improve the vehicle handling performance
.

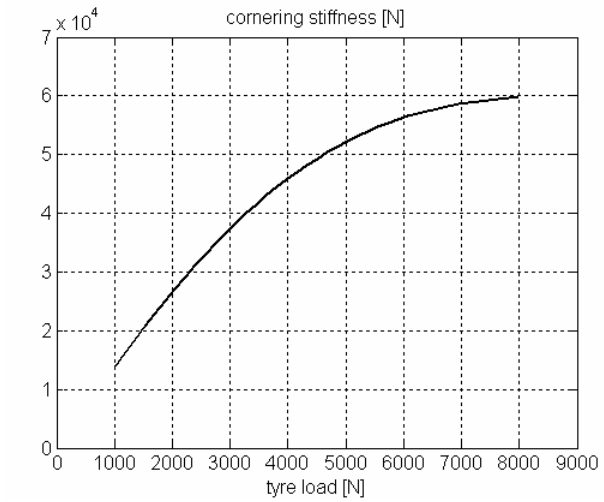

Figure 20.: Cornering stifness vs. tyre load

In figure 21, ranges of typical values of the cornering stiffness coefficient (cornering stiffness, divided by the tyre load) are shown vs. tyre load for passenger car and truck

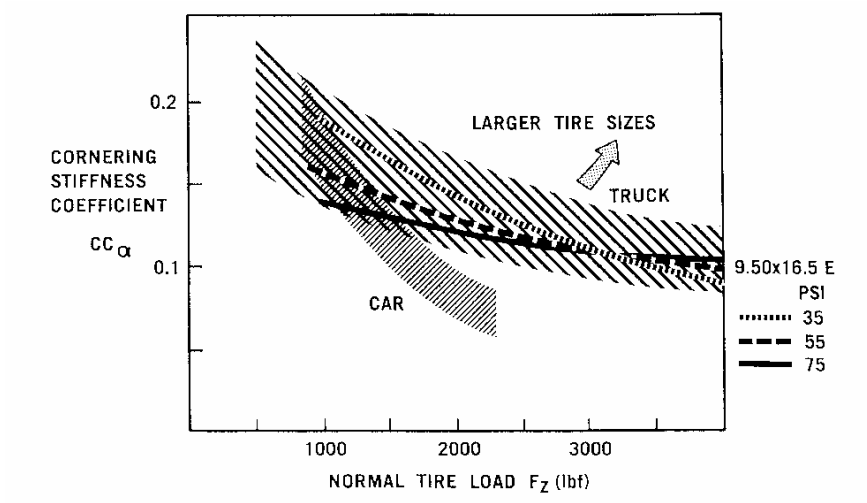

Figure 21.: Cornering stiffness coefficient (from normalized tyre force) for passenger car and truck tyres, from [2]

tyres. Truck tyres experience quite a large tyre load variation, compared to assenger car tyres. Clearly, these tyres have to be designed with minimum impact of load on tyre performance. This is illustrated in figure 21.

4.5. Pneumatic trail and aligning torque

Figure 16 indicates that the sideforce acts at a small distance behind the wheel centre. This distance is called the pneumatic trail. At small slip (small α), there is almost no sliding and the adhesion part extends almost over the entire contact area. This corresponds to a situation where the shear stress profile is very unsymmetrical along the contact area, with a rather large pneumatic trail. With slip increasing, the sliding area increases towards the front end of the contact area. Under Coulombs law, The shear stress in the sliding area follows $\mu.\sigma_z$. The normal contact stress σ_z throughout the contact area is shown in figure 22 for both a radial-ply tyre and a bias-ply tyre.

Both pictures in figure 22 confirm that the resultant vertical contact force acts slightly in front of the wheel centre (as discussed before), meaning that the pneumatic trail may even become negative for excessive sliding. Observe also the different behaviour for bias-ply and radial-ply tyres at the shoulders of the tyres. We have seen similar concentrations in shear stress in the previous sections.

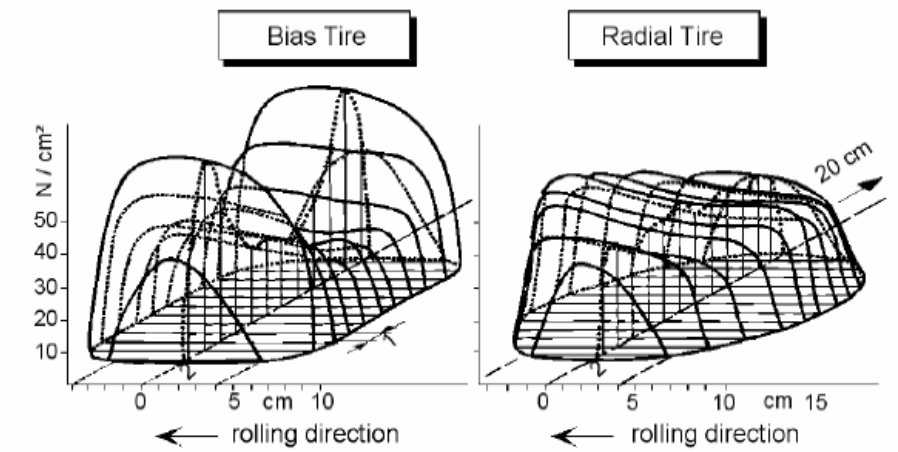

Figure 22.: Normal contact stress profile for different tyres, from [11]

Hence, we have a sideforce F_y (α) , starting at small values at $\alpha = 0$ and growing to a maximum value ($\mu.F_z$) whereas the pneumatic trail t_p (α) starts at large values, reducing to small values with even negative values for excessive slip. Pneumatic trail times sideforce yields the so-called aligning torque M_z. This torque is called aligning since it aims to orient the tyre in the speed direction. It works against the lateral deformation due to the lateral force. With:

$$M_z(\alpha) = -t_p(\alpha).F_y(\alpha) + M_{zr}(\alpha)$$

for residual torque M_{zr} (small torque resulting from inaccuracies in the tyre design, rapidly decreasing in absolute value with increasing slip angle) we expect this aligning torque to start close to zero for $\alpha = 0$, to grow in absolute value but to decrease again with the pneumatic trail for increasing slip.
We have plotted the pneumatic trail and the aligning torque in figure 23.

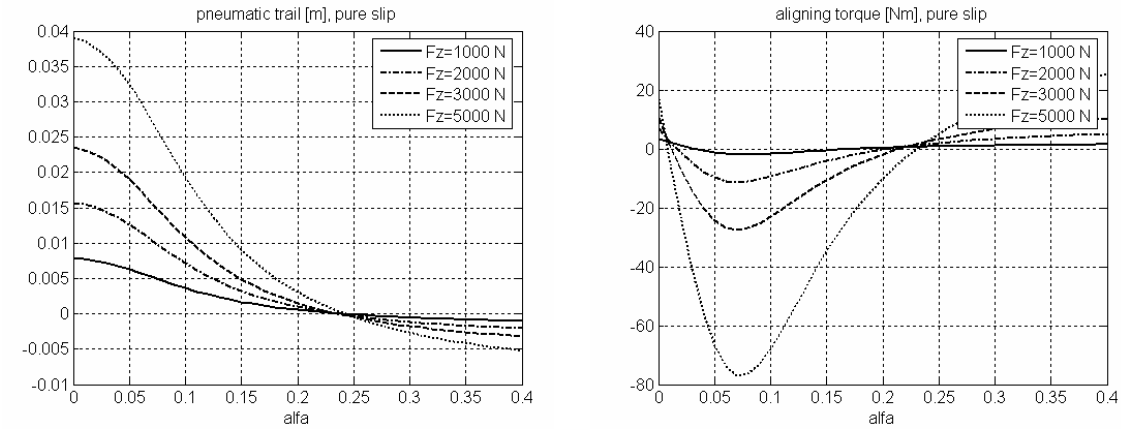

Figure 23.: Pneumatic trail & aligning torque vs slip angle

Comparing figure 23 with figure 18 (see section 4.2), we see that the aligning torque passes its maximum at a slip angle value, smaller than at the maximum of the sideforce where the tyre starts sliding. The torque from the combined effect of mechanical trail (castor) and pneumatic trail is felt by the driver through the steering wheel. Reduction of the aligning torque in absolute value should warn the driver that he or she is approaching a situation with increased risk of skidding of the front axle due to excessive understeer.

4.6. The empirical Magic Formula

Referring to the empirical Magic Formula sine version describing the lateral characteristics:

$$F_y(x) = D.\sin(C.\arctan(B.\alpha - E.(B.x - \arctan(B.x\alpha)))) + S_V$$

the different coefficients B, D and E can be expressed as follows (neglecting camber):

$$D = \mu_{yp}.F_z$$

with:

$$\mu_{yp} = (p_{yD1} + p_{yD2}.df_z) \text{ with } df_z = \frac{F_z - F_{z0}}{F_{z0}}$$

with nominal tyre load F_{z0}. Furthermore

$$BCD = p_{Ky1}.F_{z0}.\sin(2.\arctan(\frac{F_z}{p_{Ky2}.F_{z0}}))$$

$$E = p_{Ey1} + p_{Ey2}.df_z$$

$$S_H = (p_{Hy1} + p_{Hy2}.df_z)$$

$$S_V = F_z.(p_{Ky1} + p_{Ky2}.df_z)$$

4.7. Camber

So far, we neglected camber. The **camber angle** is defined as the angle between the wheel plane and the normal of the road in the transverse plane of the vehicle, see figure 24. The presence of a camber angle γ produces a lateral force, which is usually much smaller than the side force due to sideslip α. This can be explained as follows. A wheel under a camber angle would move over a circular track. The direction of motion of the wheel is forced by the vehicle velocity vector. For example, the wheel may be going straight ahead. As a result, local shear stresses arise in the contact area, building up a camber force.

For a motorcycle, the camber force is the main force between tyre and road, that prevents the tyre to slide.

In the linear range, the side force can be expressed in terms of slip angle and camber angle in the following way:

$$F_y(\alpha) = C_{y\alpha}.\alpha + C_{y\gamma}.\gamma \quad ; \text{ small } \alpha \text{ and } \gamma$$

with cornering stiffness $C_{y\alpha}$ and **camber stiffness** $C_{y\gamma}$, defined as:

$$C_{y\alpha} = \frac{\partial F_y}{\partial \alpha}(\alpha = 0, \gamma = 0) \ ;$$

$$C_{y\gamma} = \frac{\partial F_y}{\partial \gamma}(\alpha = 0, \gamma = 0)$$

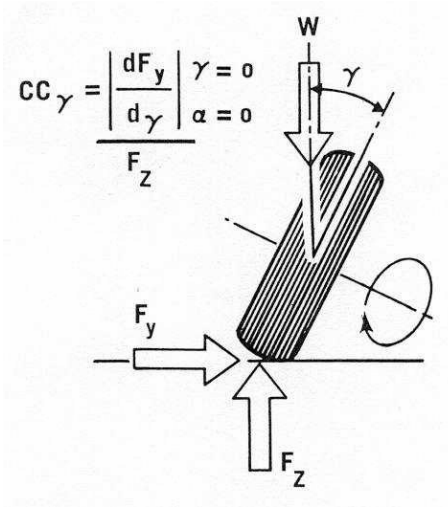

Figure 24.: Camber and camber force, from [2]

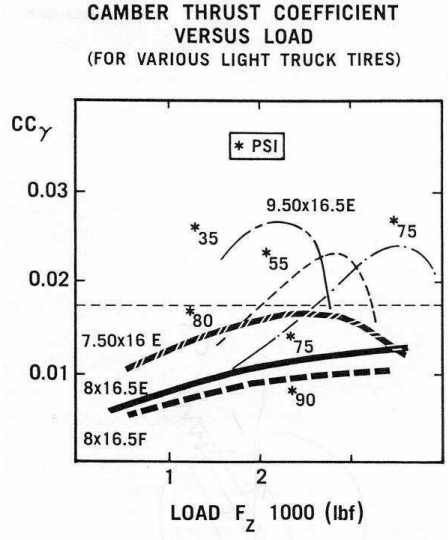

Figure 25.: Camber thrust coefficient, from [2]

For different light truck tyres, for various loads and tyre inner pressure, the camber thrust coefficient (ratio of camber stiffness and tyre load) is shown in figure 25. One observes the low value in the order of 0.01 until 0.03, to be compared to values between 0.5 and 1.0 for the normalized cornering stiffness.

In the nonlinear range, the above empirical formulas have to be corrected by including the dependency on camber. We refer to [1], [22] and [23] for further details.
We have varied the camber angle and calculated the side force, based on the Magic Formula parameters, presented in [1]. The result is shown in figure 26. The camber angle is changed such that the side force is decreased with increase of camber angle in

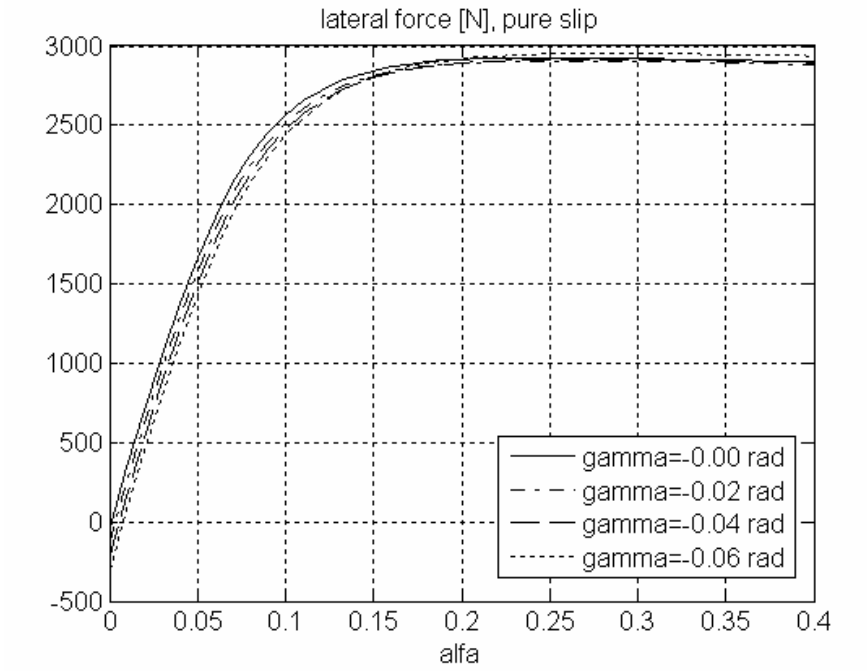

Figure 26.: Side force vs. slip angle for changing camber angle (in rad)

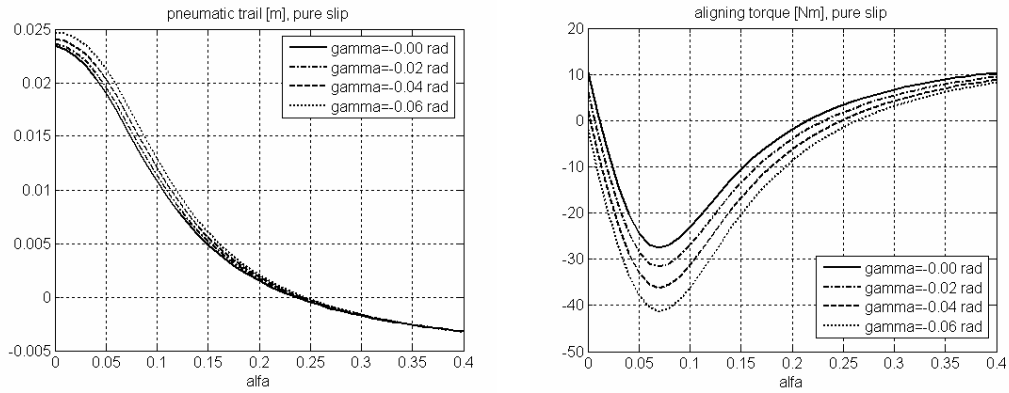

Figure 27.: Pneumatic trail & aligning torque for varying camber angle

absolute value. This is the usual case, with the carbody rolling outward, leading to a reduction of the side force. The corresponding pneumatic trail and aligning torque for varying camber angle are shown in figure 27.

4.8. The Gough plot

An interesting way of presenting tyre characteristics in a graphical way, is given by the so-called Gough-plot where side force F_y is plotted against M_z, neglecting shifts, see figure 28.

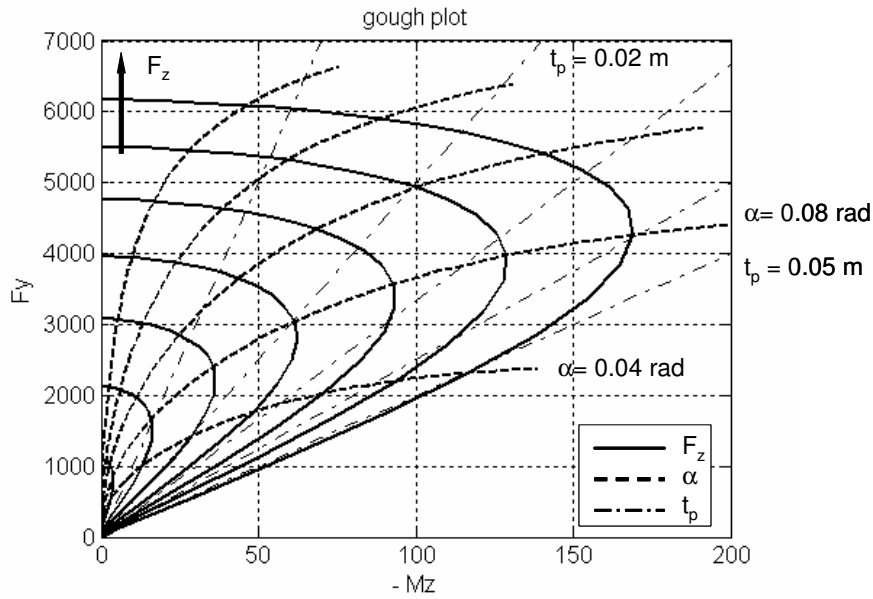

Figure 28.: Gough-plot of a passenger car tyre

(F_z = 1000 (1000) 7000, α = 0.04 (0.04) 0.2 rad, t_p = 0.01 (0.01) 0.05)

This plot is very illustrative, since it shows the dependency of the tyre characteristics on slip angle, tyre load and pneumatic trail in one picture. It clearly identifies the different impact of slip-angle (dashed) and the tyre load (solid). Lines of constant pneumatic trail are straight lines, distributed purely radial. For larger tyre load, the lateral force increases. The aligning torque increases as well, but it starts to decrease in slip angle, when the lateral force is still increasing in the slip angle. For larger slip angle, also the side force starts to saturate.

This plot shows that already for small side force and aligning torque (i.e. normal non-extreme cornering), a clear distinction can be made between the impact of α and F_z, the latter of which is close to the impact of road friction. Consequently, this plot suggests itself as a way of monitoring side slip and road friction from the tyre performance, a fact that has been exploited successfully by Pasterkamp [28].

5. Combined braking and cornering

The discussion in the preceding section deals with pure slip, i.e. in cases where the car is either cornering, or braking/driving. When a driver torque or brake torque is applied during cornering, the total horizontal force is acting not in the longitudinal or lateral direction, and the cornering force is reduced. Likewise, applying a side force while braking or driving will reduce the longitudinal force, i.e. the braking or driving potential of the tyre. With the total force:

$$F_{tyre} = \sqrt{F_x^2 + F_y^2}$$

we can define the resultant force coefficient as

$$\mu_{tyre} = \frac{F_{tyre}}{F_z}$$

We have plotted the longitudinal and lateral force versus longitudinal slip in figure 29, for varying slip angle.
One observes a decrease of F_x and increase of F_y for increasing slip angle.

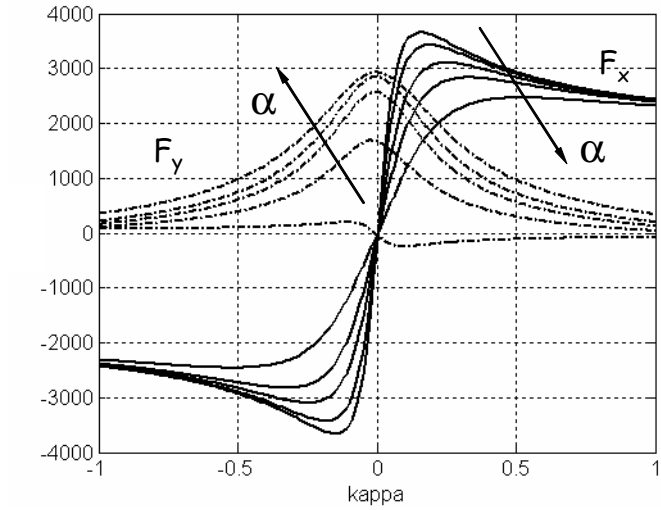

Figure 29.: Interaction between longitudinal forces and side forces

For small brakeslip or driveslip, the sideforce is dominant. For large brakes;lip or driveslip, there is hardly any potential left for the sideforce, and the sideforce appears to be small compared to values for small longitudinal slip.

5.1. Polar diagrams, F_x vs. F_y and F_x vs. M_z

In figure 30, we have included so-called polar plots, with F_x plotted against sideforce F_y

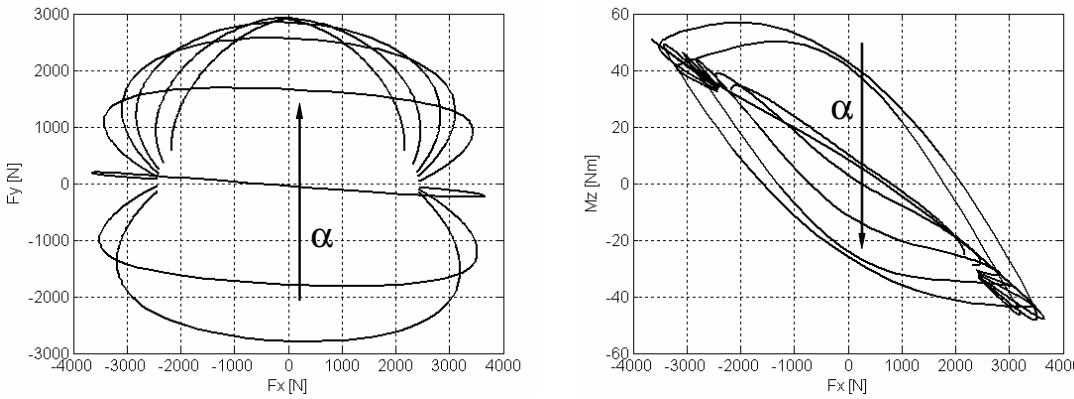

Figure 30.: Polar diagrams, F_x vs. F_y and F_x vs. M_z for constant slip angle

(α=-0.1 -0.05 0.0 0.05 0.1 0.15 0.25 0.4)

and against aligning torque M_z, respectively.
These diagrams are nonsymmetrical in F_x , which is due to the carcass-stiffness. The longitudinal force, acting in the contact zone in the direction of the local rotated longitudinal coordinate axis, contributes to both the total lateral force F_y and to the aligning torque M_z. Clearly, this works out just opposite when the side force changes sign.
Observe in figure 30 that the F_x-F_y diagram is close to a circular area. One would expect the saturation of the total horizontal force F_{tyre} to occur when $F_{tyre} = \mu.F_z$ with road friction μ. This would exactly lead to a circle, describing the maximum possible values for F_{tyre}.

5.2. The Magic Formula for combined slip.
The magic Formula describes combined slip using weighting functions for the pure slip characteristics:

$$F_x(\alpha,\kappa) = G_{x\alpha}(\alpha,\kappa).F_{x,pure}(\kappa)$$
$$F_y(\alpha,\kappa) = G_{y\kappa}(\alpha,\kappa).F_{y,pure}(\alpha) + S_{Vy\kappa}$$
$$M_z(\alpha,\kappa) = -t_p(\alpha_{t,eq}).(F_y(\alpha,\kappa) - S_{Vy\kappa}) + M_{zr}(\alpha_{r,eq}) + s.F(\alpha,\kappa)$$

for equivalent slip angles $\alpha_{t,eq}$ and $\alpha_{r,eq}$ (depending on longitudinal slip), residual torque M_{zr} and moment arm s of F_x contributing to M_z. See [23] for more details. Again we observe a contribution to the aligning torque from the longitudinal force, due to the carcass flexibility.
The weighting functions in the above expressions can be described by cosine versions of the Magic Formula, with Magic Formula parameters tuned from experiments.
It can be shown (see for example [23] and [10]) that the combined slip forces can be approximated well by:

$$F_x(\alpha,\kappa) \approx \frac{\rho_x}{\rho}.F_{x,pure}(\rho) \quad ;$$
$$F_y(\alpha,\kappa) \approx \frac{\rho_y}{\rho}.F_{y,pure}(\rho) \quad ; \ \rho = \sqrt{\rho_x^2 + \rho_y^2}$$

for theoretical slip values ρ_x and ρ_y, introduced earlier. A similar successful approximation can be derived from the practical slip quantities:

$$F_x(\alpha,\kappa) = \frac{\kappa}{s}.F_{x,pure}(s) \quad ;$$
$$F_y(\alpha,\kappa) = \frac{\tan(\alpha)}{s}.F_{y,pure}(s) \quad ; \ s = \sqrt{\kappa^2 + \tan^2(\alpha)}$$

We refer to [29] where these approximations have been studied in detail.

Some results are shown in figure 31 where the polar plot F_x vs. F_y and both tyre forces vs. longitudinal slip for approximations cf. Magic Formula and cf. the above similarity approach are shown. We observe the unrealistic symmetry in the approximation. On the other hand, both type of curves are not far apart, and one should realize that the approximated curves are based on the pure slip characteristics, i.e. they do not require combined slip measurements. And if more accurate results are needed, the approximated curves give a very good first estimate, to verify the test results. Note that,

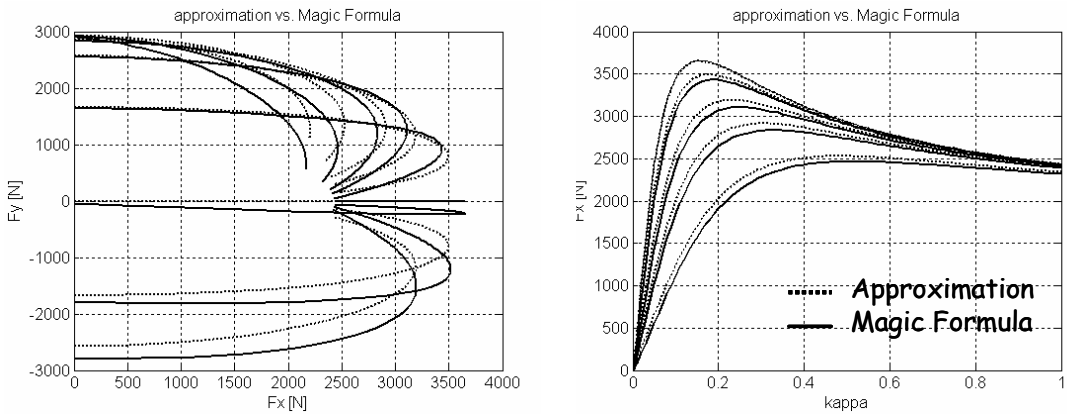

Figure 31.: Approximation combined slip characteristics based on pure slip characteristics vs. Magic Formula

in many analyses, the high accuracy from the Magic Formula empirical approach are not required, and the approximated values may serve as a good alternative. Pure slip characteristics are often easily estimated from published graphs, i.e. even pure slip measurements may not be necessary to find a satisfactory description of the pure slip characteristics, and through that, a combined slip description.

5.3. Physical tyre models, requirements

We have mentioned earlier two possible approaches to derive **physical tyre models**:

1. the brush model
2. the stressed string model

These two important physical models are schematically shown in figure 32.
These approaches are two special examples of more general physical models, which will be discussed here in some more detail with special emphasis to brush models. The models all give a general description of the tyre under full combined slip conditions. Therefore, these models will be addressed in this section. Note however, that the models can easily be simplified to pure slip in either lateral (i.e. cornering) or longitudinal (i.e. braking or driving) direction.

Physical models should account for:

- frictional properties in the tyre-road interface
- distribution of the normal contact force

- stiffness of the tread rubber
- stiffness of the carcass.

Models of the carcass commonly encountered in the tyre literature can either be a spring, they can be of beam type or of stretched string type. The exact representation of the carcass by a beam instead of a stretched string is more difficult because of the fact that the differential equation for the shape of the deformed peripheral line of the carcass

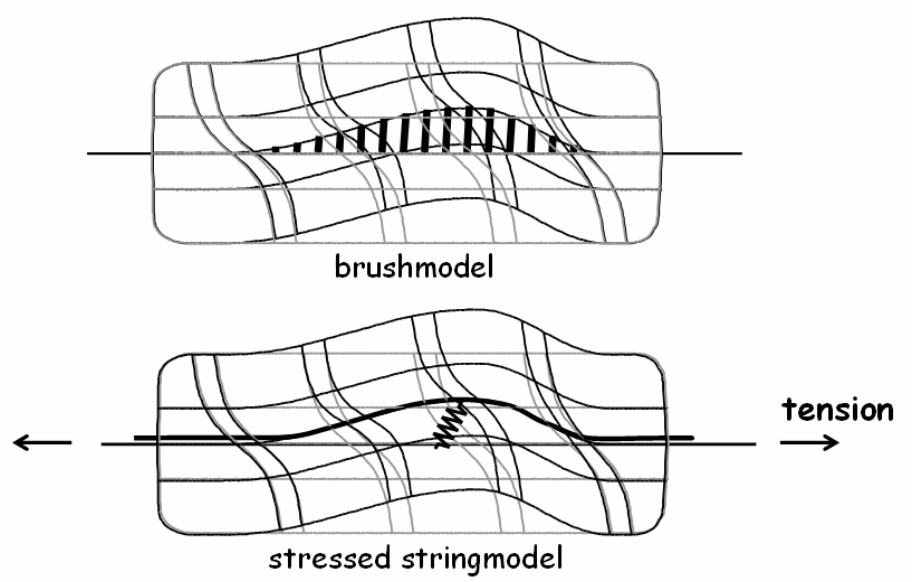

Figure 32.: Physical tyre models (brush-model, stressed string model)

becomes of fourth instead of the second order. For the study of steady state tyre behaviour, most authors approximate the more or less exact expressions for the lateral

As an extension of the model of Fromm (brush approach) and of Julien (see [15] for further references) who did not consider carcass elasticity, Fiala [6] and Freudenstein [9] developed theories in which the carcass deformation has been approximated with a symmetric parabola determined only by the lateral force. Böhm [3] and Borgmann [4], the latter without tread elements, use asymmetric approximate shapes determined by both the lateral force and the aligning torque. In [24] and [25], Pacejka describes the steady-state tyre characteristics for a stretched-string tyre model with and without tread elements attached to the string. The lateral stiffness distributed as measured on a slowly rolling tyre in terms of influence of Green's functions (cf. [31]) may be employed in a model for the slipping tyre as has been discussed in [26] and [27].
The combination of stressed string model and brush-model under arbitrary combined slip conditions has been considered by [30]

5.4. Performance of different physical tyre models

Frank [7] has carried out a thorough comparative investigation of the various one-dimensional models. He employed a general fourth-order differential equation with which stretched string, beam and stretched beam tyre models can be examined. He

obtained the exact solution of the stationary side slip problem (no longitudinal slip included), and comparison with the various tyre models revealed that the stretched string type of model was more suitable for the simulation of bias-ply tyres, whereas the beam model (i.e. with belt-bending taken into account) was more appropriate for the radial-ply tyre.
The following models were compared:

a. stretched beam model. The belt is taken as a beam under tension, i.e. with bending stiffness taken into account.
b. beam model. Similar to model a, however with the tension force neglected.
c. approximate solution for the lateral force by Fiala, see [6].
d. model of Fromm, taking only tread deformation into account with the carcass assumed to be rigid.

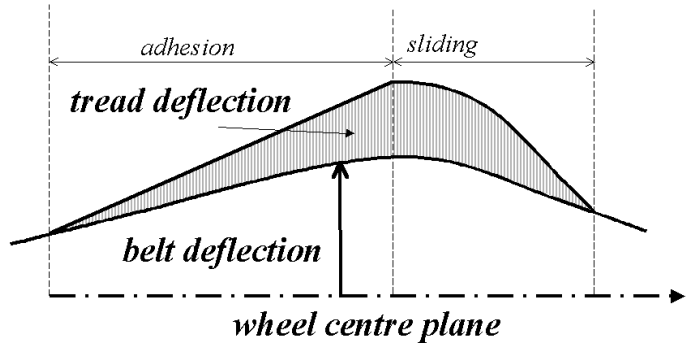

Figure 33.: Lateral tyre deformation

Before we discuss the results, we first give some understanding about belt models. Consider the tyre top-view shown in figure 33.

Distinction is made between belt deflection and tread defection. The belt deflection can, in general, be described by a stretched beam. That means that the steady state lateral displacement y(x) of the belt, in terms of the position x along the wheel centre plane, satisfies a fourth order differential equation:

$$EI.\frac{d^4y}{dx^4} - S.\frac{d^2y}{dx^2} + K.y = q_y(x)$$

for bending stiffness EI, tension force S, carcass stiffness per unit length K and lateral side force per unit length $q_y(x)$. With S = 0, the beam is non-stretched. For EI = 0, the equation reduces to the stretched string equation. The Fiala approximation describes the lateral force F_y as a third order expression in the slip angle α. The model of Fromm neglects the carcass deflection, i.e. only tread deflection is described leading to the brush model.
Figures 34 and 35 present the calculated characteristics (taken from [9]) of models a – d.

The parameters in cases a – c were chosen in such a way as to give a best fit to

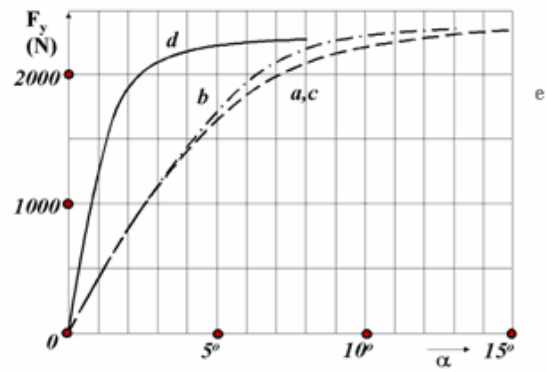

Figure 34.: Cornering force, model a – d

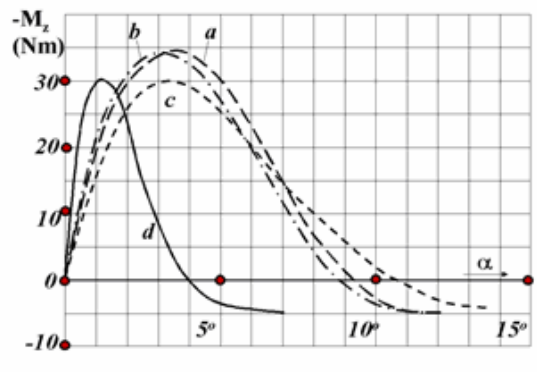

Figure 35.: Aligning torque, model a - d

experimental data for the cornering force at small slip angles. The curves d show the result when carcass elasticity has been neglected. The coefficient of friction μ was taken constant and the vertical pressure distribution was taken from measurements, lying between a parabolic and an elliptic shape. The positive aligning torque at high slipvalues arose due to a slightly asymmetric shape of the pressure distribution $\sigma_z(x)$. The phenomenon that in practice the aligning torque indeed varies in this way is probably due to a combination of several effects. Apart from the cause just mentioned above, the rolling resistance force acting out of the wheel plane (along the actual deformed belt, out of the wheel plane cf. figure 32), may contribute. Another important factor causing the moment to become positive is the fact that the coefficient of friction is not a constant but may depend on the sliding velocity as we shall see later. That means that the coefficient of friction will change (may decrease) in the sliding part of the contact area, which also causes the slight drop in the $F_y(\alpha)$ – curves as has sometimes been found experimentally at high slip values especially on wet roads.
The influence of different but symmetric shapes for the vertical force distribution along the x-axis has been theoretically investigated by Borgmann [4]. He finds that, especially for tyres exhibiting a low carcass stiffness, the influence of the pressure distribution is of importance and has, as may be expected, particular effect on the aligning torque at higher values of slip angle α.
Many authors adopt the parabolic normal stress distribution in the contact area for purpose of mathematical simplicity, or a uniform (rectangular) distribution.
Figures 34 and 35 show that, when the model parameters are chosen properly, the choice of the type of carcass model hardly influences the results.

5.5. The Brush model

For illustration, we shall present now the theory of steady-state slip with the aid of the simple brush-type tyre model, originally stemming from Fromm. The theory of this section will not consider camber and turning (turnslip) of the wheel. See [23] for an extensive treatment of the brush-model. We refer to figure 36 for a schematic layout of the model. The tyre is equipped with small linear beams (brush elements), some of

which touch the ground and, as a result, will be deformed as a linear beam. Two regions are identified, a leading adhesion region where the contact line (connecting the tips of the brush elements) is straight, and a sliding region where the shear stress

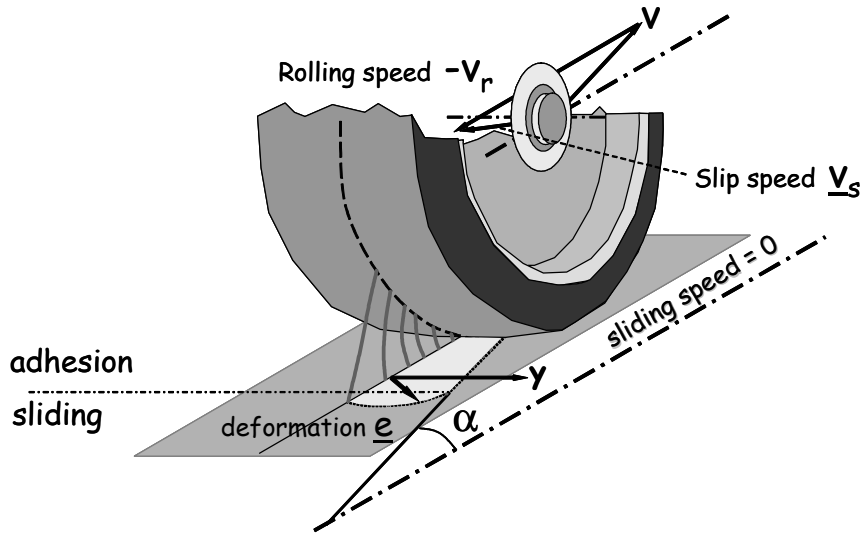

Figure 36.: The brush-model (according to Fromm)

follows Coulombs law:

$$\tau = \sqrt{\tau_x^2 + \tau_y^2} = \mu.\sigma_z$$

The tyre is moving with speed V, built up from a rolling speed V_r and a slip speed V_s, with both a lateral and a longitudinal component. The tyre is assumed to move sideways with a slip angle α, in combination with a longitudinal slip κ, i.e. we assume the general case of combined slip.

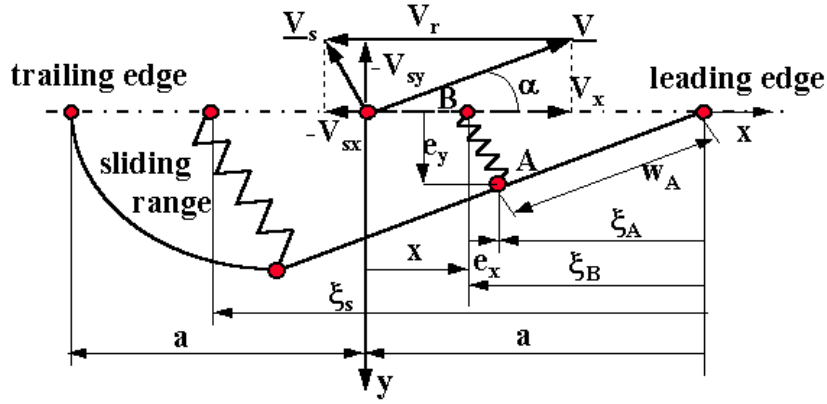

Figure 37.: Topview brush model

A topview of the tyre under deflection of the tread elements (the bristles, or brushes) is shown in figure 37.

5.5.1. Displacements in terms of slip and position.

At the leading edge of the contact area, the deformation is still zero. The base and the tip of the tread element coincide. With the tyre moving with speed V and rolling with rolling speed V_r, the base of the tread is attached to the wheel plane and will move inside the contact area with the rolling speed, say to point B. At the same time, the tip of the tread element will move to point A opposite to speed V. With time-interval Δt, this means that the displacement w_A in the actual contact area along the deformed treads can be written as:

$$w_A = V.\Delta t$$

The new positions ξ_A (tip) and ξ_B (base) are found from:

$$\xi_A = V.\cos(\alpha).\Delta t$$

$$\xi_B = V_r.\Delta t$$

from which expressions for the deformation e_x and e_y (cf. figure 37) can be derived:

$$e_x = [V_r - V.\cos\alpha].\Delta t$$

$$e_y = V.\sin\alpha.\Delta t$$

This means that the displacements can be expressed in terms of either the position in the deformed belt situation, ξ_A, or in the undeformed belt co-ordinate ξ_B as follows:

$$\begin{pmatrix} e_x \\ e_y \end{pmatrix} = \begin{pmatrix} \dfrac{V_r - V_x}{V_x} \\ \tan\alpha \end{pmatrix}.\xi_A = \begin{pmatrix} \dfrac{V_r - V_x}{V_r} \\ \dfrac{V_x}{V_r}.\tan\alpha \end{pmatrix}.\xi_B$$

The vector of coefficients corresponds to either practical slip and theoretical slip, as defined before. The expressions are of the general form:

displacement = slip x position

where slip is defined on the basis of either the position ξ_A with respect to the deformed tyre or the position ξ_B with respect to the undeformed tyre. This conforms our earlier statement that practical slip quantities are related to the deformed tyre quantities

whereas the theoretical slip quantities are derived on the basis of undeformed tyre quantities.

The contact area is taken as a square with length 2.a and width 2.b. We assume a parabolic pressure distribution p(x), taken uniform over the contact width 2.b:

$$\sigma_z(x) = \sigma_{z0}.[1-\left(\frac{x}{a}\right)^2]$$

with σ_{z0} following from the condition that

$$F_z = \int_{-b}^{b}\int_{-a}^{a}\sigma(x)dx.dy$$

and thus

$$\sigma_{z0} = \frac{3.F_z}{8ab}$$

5.5.2. Adhesion and sliding

We shall now derive expressions for the total displacement e = $\sqrt{e_x^2 + e_y^2}$ in the contact area, with distinction between adhesion and sliding.
In the **adhesion region**, it follows that

$$e = \rho.\xi_B = \frac{1}{1+\kappa}.[\sqrt{\kappa^2 + \tan^2\alpha}].\xi_B$$

In the **sliding region**, assuming Coulomb friction with friction coefficient μ, the shear stress $\tau(x,y)$ is bounded by $\mu.\sigma(x)$. The displacement e is therefore bounded as well, and it follows from the stiffness of the tread, denoted as k

$$e = e_{\max} = \frac{\tau(x,y)}{k} = \frac{\mu.\sigma_z(x)}{k} = \frac{3.\mu.F_z}{8.a^3b.k}.(a^2 - x^2)$$

We introduce the **tyre parameter** θ by

$$\theta = \frac{4}{3}.\frac{a^2b.k}{\mu.F_z}$$

resulting in

$$e_{\max} = \frac{\xi_B(2a - \xi_B)}{2a.\theta}$$

The break-away point ξ_s (indicated in figure 37) at which adhesion turns into sliding is found by taking e_{max} equal to the deformation e yielding:

$$\xi_s = 2a.(1 - \theta.\rho)$$

Consequently, for $\rho = 0$, $\xi_s = 2a$ and the full contact area is in the state of adhesion. With increasing ρ, the break away point ξ_s moves to a value $\xi_s = 0$, attained at $\rho = 1/\theta$. In other words, the parameter $\theta > 1$ is the reciprocal total slip for which the full contact area is just sliding. Beyond the magnitude $1/\theta$. for total theoretical slip, the tyre remains in a state of complete sliding.
In case of pure slip, this situation is reached for either

$$|\alpha| = \alpha_m = \arctan(1/\theta)$$

or

$$\kappa_m = \frac{1}{\theta - 1}, \text{ in case of driving } (\kappa > 0)$$
$$\kappa_m = -\frac{1}{\theta + 1}, \text{ in case of braking } (\kappa < 0)$$

5.5.3. Shear forces
Next, we determine the shear stresses and, from that, the shear force.
The shear stressses are found from

$$\underline{\tau}(\xi_B) = \underline{\tau}_a(\xi_B) = k.\underline{e} = -k.\xi_B.\underline{\rho} \quad ; \text{adhesion region, } \underline{\rho} = \begin{pmatrix} \rho_x \\ \rho_y \end{pmatrix}$$

$$\underline{\tau}(\xi_B) = \underline{\tau}_s(\xi_B) = \mu.p(x).\frac{\underline{\rho}}{\rho} = -k.e_{\max}(\xi_B).\frac{\underline{\rho}}{\rho} \quad ; \text{sliding region}$$

where it was used that for isotropic tread stiffnesses, the shear stress vector has the same (opposite) orientation as the theoretical slip vector.
The shear force is now easily calculated from

$$\underline{F}_{shear} = 2.b.[\int_0^{\xi_s} \underline{\tau}_a(\xi_B)d\xi_B + \int_{\xi_s}^{2a} \underline{\tau}_s(\xi_B)d\xi_B]$$

and the force-components (lateral force, longitudinal force) are obtained from:

$$\underline{F}_{shear} = -\frac{\rho}{\rho}.F \equiv -\frac{\rho}{\rho}\sqrt{F_x^2 + F_y^2}$$

Remark

Note that this expression has been used for the empirical Magic Formula to approximate the horizontal contact forces from the pure slip characteristics. We observed earlier that both this approximation based on theoretical slip as the approximation based on practical slip both give satisfactory results.

We easily arrive at:

$$\begin{aligned} F &= \mu.F_z.[3.\theta.\rho - 3.(\theta.\rho)^2 + (\theta.\rho)^3] \quad ; \rho < 1/\theta \\ &= \mu.F_z \qquad\qquad\qquad\qquad\qquad\quad ; \rho \geq 1/\theta \end{aligned}$$

5.5.4. Aligning torque and pneumatic trail

In the same way, one arrives at a closed form expression for the aligning torque M_z :

$$\begin{aligned} M_z &= 2.b.\int_0^{2a} \tau_y(\xi_B).(a - \xi_B)d\xi_B = \\ &= \frac{\rho_y}{\rho}.\mu.F_z.a.[\theta\rho - 3(\theta\rho)^2 + 3(\theta\rho)^3 - (\theta\rho)^4] \quad ; \rho < 1/\theta \end{aligned}$$

In case $\rho \geq 1/\theta$, M_z will vanish. Note that this can either be a result of increasing slip angle α or increasing brakeslip or driveslip $|\kappa|$. The pneumatic trail follows from the ratio of F_y and $-M_z$:

$$\begin{aligned} t(\rho) &= \frac{1}{3}.a.\frac{1 - 3\theta\upsilon + 3(\theta\rho)^2 - (\theta\rho)^3}{1 - \theta\rho + (\theta\rho)^2/3} \quad ; \rho < 1/\theta \\ &= 0 \qquad\qquad\qquad\qquad\qquad\qquad\quad ; \rho \geq 1/\theta \end{aligned}$$

5.5.5. Tyre characteristics according to the brush model

The longitudinal and lateral forces under pure slip conditions are shown shown in figure 38, where we have choosen:

$k = 2.10^7$ [N/m^3]
$b = 0.1$ [m]

and have used the following approximate relationship between tyre load F_z and half contact length a (see also [35]):

$a = 0.0011\sqrt{F_z}$ [m]

with Fz in N.

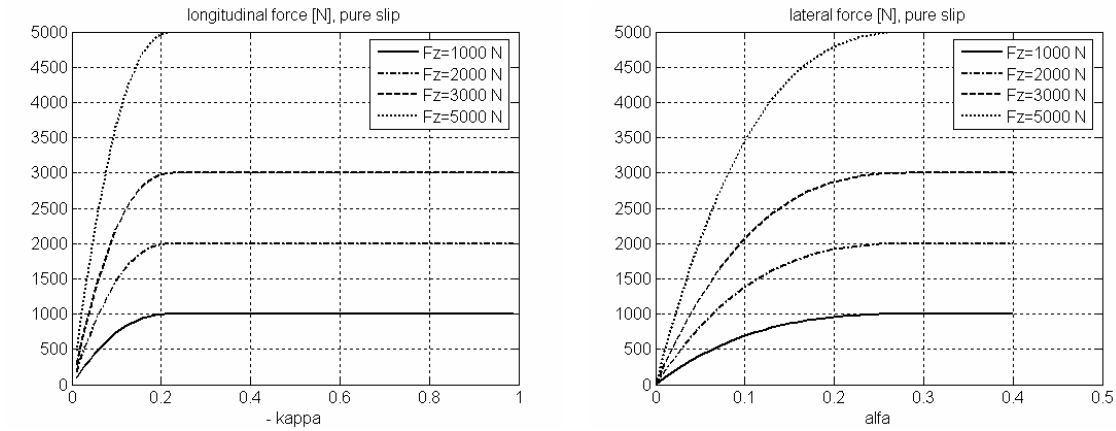

Figure 38.: Longitudinal and cornering tyre characteristics, based on the brush model.

One observes the side force F_y to be a monotonous curve, reaching the saturation level $F_y = \mu.F_z$ at $\alpha = \arctan(1/\theta)$. No slope reversal occurs, as observed in experimental results. A similar behaviour is observed for the longitudinal force. Corresponding trail

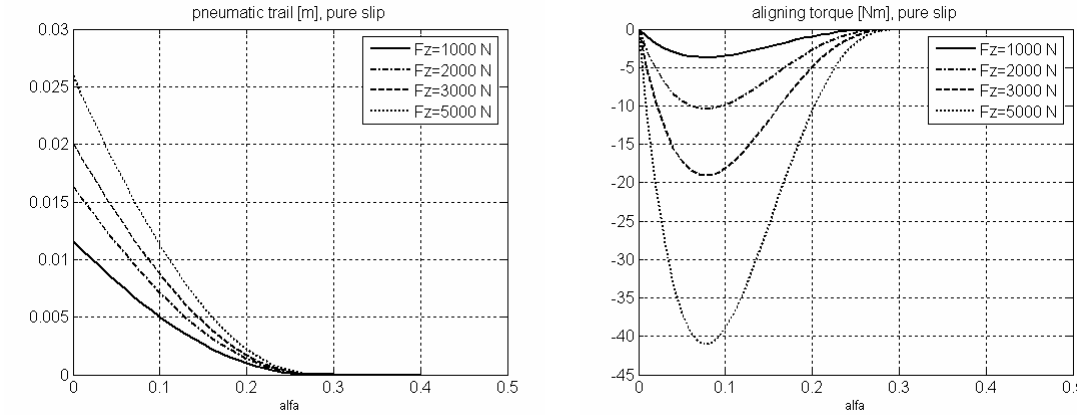

Figure 39.: Pneumatic trail & aligning torque vs slip angle

and aligning torque are shown in figure 39.

The aligning torque reaches a peak at $\alpha=\arctan(1/(4.\theta))$, after which it reduces in absolute size to reach a zero value at $\alpha = \arctan(1/\theta)$. The aligning torque does not change sign with increasing slip angle in contrast to the earlier presentations of the aligning torque.

The pneumatic trail is a monotonous function in α, starting with a nonzero slope at $\alpha = 0$. Again, it tends to zero, which value is reached at $\alpha = \arctan(1/\theta)$. Its value at vanishing slip angle:

$$t(0) \to \frac{a}{3} \; ; \alpha \downarrow 0$$

is smaller then normally encountered (around 0.5a).

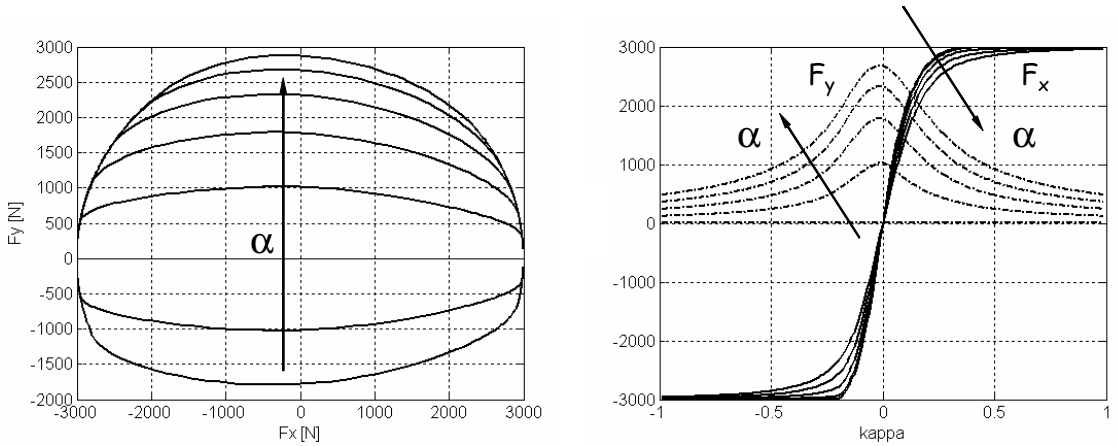

Figure 40.: Polar plot (F_x vs. F_y), and interaction between longitudinal forces and side forces, for the brush model.

We note here that the variation of the tyre forces in the tyre load F_z is different from experimental results. It can be shown that F_x and F_y vary proportionally in F_z (i.e. no degressive relationship). The aligning torque varies proportionally with $F_z \cdot \sqrt{F_z}$.

5.5.6. Brush model including carcass compliance

The combined slip characteristics are shown in figure 40 in terms of the F_x - F_y polar plot and the longitudinal and lateral forces versus longitudinal slip. The polar plot is close to being symmetrical around F_x = 0. A similar symmetry turns out to be present in the olar plot of M_z vs. F_x. In order to remove this symmetry (compare with figure 30), one may include the carcass compliance, as indicated in figure 41. The carcass symmetry plane is connected to the undeformed symmetry plane with lateral and longitudinal springs. The longitudinal and lateral forces now contribute to the moment around point C

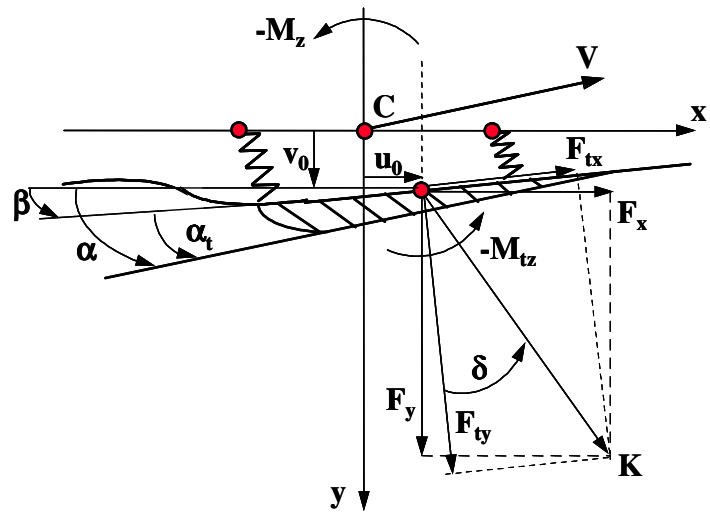

Figure 41.: Including carcass compliance

(centre of contactarea with slip absent).
It is assumed that the local behaviour in the contactarea for the deflected carcass can be described by the brush-model as described above.
We have plotted M_z vs. F_x for both cases, without and including the carcass compliance, in figure 42.

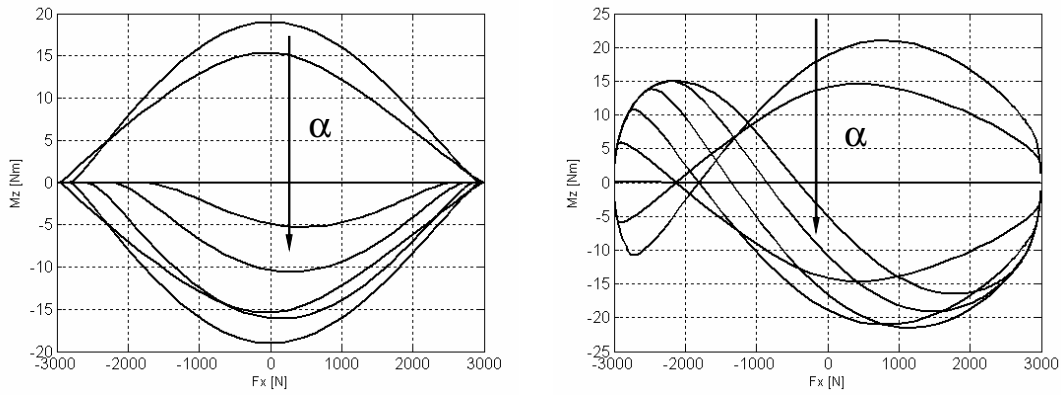

Figure 42.: Polar plot (F_x vs. M_z), for nondeflected carcass (left) and deflected carcass (right).

One observes that the symmetry is lost, but that the behaviour is still different from figure 30. Also the order of magnitude is different (lower) and the Magic Formula data show nonzero values for large longitudinal slip, being due to the residual torque, the nonzero values of the trail for large slip and especially the contribution of the longitudinal force in the aligning torque for combined slip (nonzero moment arm s of F_x contributing to M_z, see the Magic Formula expressions introduced earlier). The brush-model for deflected carcass necessarily leads to zero aligning torque for large slip, corresponding to the right and left ends of the graphs in figure 42. In between, however, the F_x vs. M_z graphs may be made more steep by tuning the carcass-compliance, especially by reducing the lateral carcass stiffness.

5.6. The brush string model

In [29], the brush model has been combined with a stretched string model, as indicated in figure 43. This model is referred to as the brush-string model, in contrast to the bare string model, applied extensively by Higuchi, see [16]. A bare stretched string model consists of an endless string which is kept under a certain pretension by a uniform radial force distribution, comparable with inflation pressures in real tyres. This string is elastically supported to the wheel centre plane. The deflection in the contact area can be described by two second order differential equations, of the form:

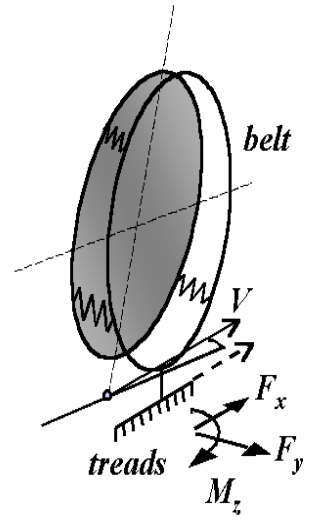

Figure 43.: The combined brush - string model

$$\sigma_y^2 . \frac{\partial^2 u_y}{\partial x^2} - u_y = -\frac{q_y}{c_{cy}} q$$

with lateral deflection u_y, local shear force q_y (sheer stress, integrated over de tyre width), relaxation length σ_y, and carcass stiffness per unit length c_{cy}. Likewise in the longitudinal direction. For points of the string outside the contact area, q_y is taken equal to zero. Under steady state conditions, one may derive for a rotationally symmetric elastic body representing a wheel and tyre rolling over a smooth surface that

$$V_g = -V(1+\kappa).\left(\zeta_y + \frac{du_y}{dx}\right)$$

with local sliding speed V_g, theoretical slip ζ_y (likewise in x-direction). This means that, in the adhesion area, the x-derivative of the local deflection is described by the tyre slip. As observed earlier, in the sliding area, the total shear stress vector is described by the normal tyre stress through Coulomb's law.
The above equations describe the **belt deflection** and the **contact phenomena**, respectively. In fact, this distinction can be made for any model-based tyre handling analysis.
As a result, one is left with a set of equations, that can be solved in a straightforward way. The extension of the bare - string model to the brush - string model leads to slightly more complex equations, but the basis is the same. It involves the inclusion of the tread stiffnesses k, denoted here as c_p.

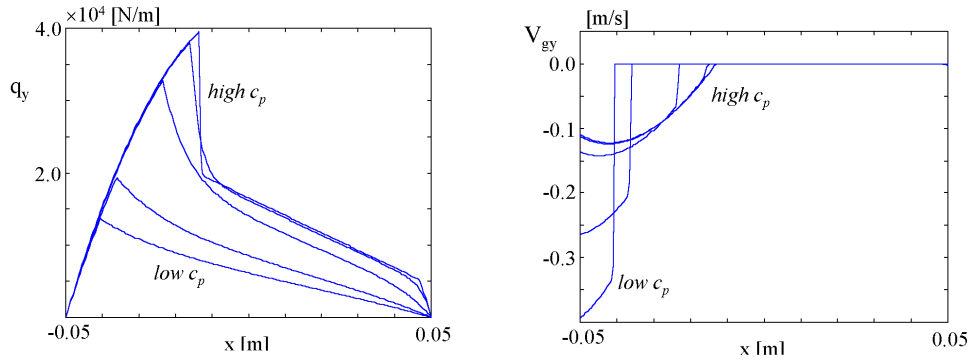

Fig.: 44.: Shearforces, sliding speeds for small relaxation lengths, (κ;α) = (0.02, 0.04)

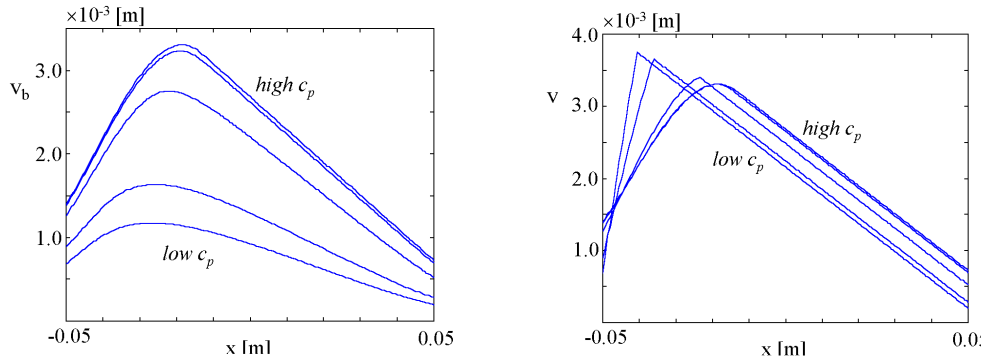

Fig.: 45.: Belt and total deflections for small relaxation lengths, (κ;α) = (0.02, 0.04)

It is of interest to examine the tyre performance for varying treadstiffness where one would expect a 'brush-type' behaviour for much lower treadstiffness whereas a 'bare belt-type' behaviour is likely to occur for much larger treadstiffness. This has been investigated for the case of small relaxation length.
Results for fixed small (combined-) slipvalues are shown in figures 44 – 45, restricting to the lateral properties only.
The following observations can be made when the treadstiffness is reduced from very stiff (i.e. with a tyre behaving as a stretched string) to very soft (i.e. with a tyre behaving like a rigid wheel with brushes) with the slipvalues and tyreload unchanged. The total deflection remains more or less unchanged (at least in order of magnitude) whereas the beltdeflection is strongly reduced (and hence the tread deflection strongly increased). The shape of the total deflection over the contact area changes from rather smooth (dominated by beltdeflection) to a shape with a sharp transition between adhesion and rearward sliding region.

For high treadstiffness, two sliding regions are found with the one at the front side of the contact area being very small (in our example about 3 % of the total contact area). With increasing treadstiffness, the transition of the sliding speeds between sliding and adhesion regions becomes less severe. The adhesion area is enlarged with softer treads, at the cost of higher sliding speeds in the rear sliding region. In other words, softer treads increase the cornering and braking potential of the tyre (e.g. wintertyres versus all-season tyres).

6. Transient and dynamic performance

For fast maneuvering of the vehicle, the rubber elements in the contact area will not follow the behaviour at the axle instantaneously. This phenomena, known as **transient behaviour**, can best be described by a first order equation:

$$\frac{\sigma_y}{V_r}\cdot\frac{d}{dt}\zeta_{y,area}+\zeta_{y,area}=\zeta_{y,axle}$$

for theoretical slips $\zeta_{y,area}$ and $\zeta_{y,axle}$ at the contact area and the axle, respectively, relaxation length σ_y and rolling speed V_r. The relaxation length is found to be well approximated by:

$$\sigma_y = \frac{1}{C_{cy}} . \frac{d}{d\alpha} F_y(\alpha)$$

with lateral tyre slipforce F_y in slip angle α, and lateral carcass stiffness C_{cy} (describing lateral force vs. lateral deflection for a non-rotating tyre fixed to the ground). The relaxation length is in the order of 2 – 3 times half the contact length, for small slip angle. The above relationship indicates that the relaxation length depends on the slip angle.
A similar discussion can be held for longitudinal transient behaviour, resulting in a similar equation.

6.1. Belt dynamics

The transient phenomena are relevant up to an input loading frequency of about 8 Hz. With higher frequencies, belt dynamics may become important. The first vibration modes are related to oscillations of the tyre belt as a rigid ring with respect to the wheel axle. Mainly the side wall stiffnesses are responsible for the tyre behaviour, with these rigid belt modes having frequencies up to about 90 – 100 Hz. Beyond these frequency, flexible eigenmodes start to arise, with belt deflections varying close to harmonically around the tyre circumference. In contrast to transient behaviour, these phenomena (rigid-ring and flexible ring deflections) are referred to as **dynamic tyre behaviour**. The in-plane and out-of-plane dynamic tyre behaviour has been extensively studied by Zegelaar, Maurice and Schmeitz (see list of references for their theses). For the in-plane behaviour, rigid ring vibration modes are found in [35] for a free tyre for frequencies of about 48 Hz (circumferential, in phase with rim-rotations), 106 Hz (circumferential, out of phase with rim rotations) and 98 Hz (vertical translational modes). The first flexible mode starts to occur at about 92 Hz.
Some standing tyre modes are shown in figure 46 (from [35]).

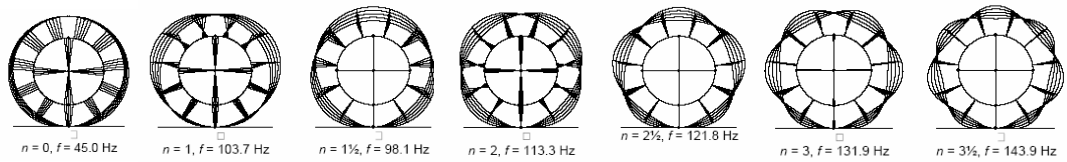

Figure 46.: Mode shapes (in-plane) for a standing tyre

For the out-of-plane behaviour, one observes, for a free tyre, rigid ring mode shapes at around 40 – 45 Hz (lateral, camber, yaw mode shapes). The frequencies for modes of a tyre standing on the road appear to be close to the modes of a free tyre.

The relevance of transient behaviour (up to about 8 Hz) and dynamic tyre behaviour (beyond 8 Hz) is schematically shown in figure 47, taken from the MF-Tyre and MF-Swift manual [19]:

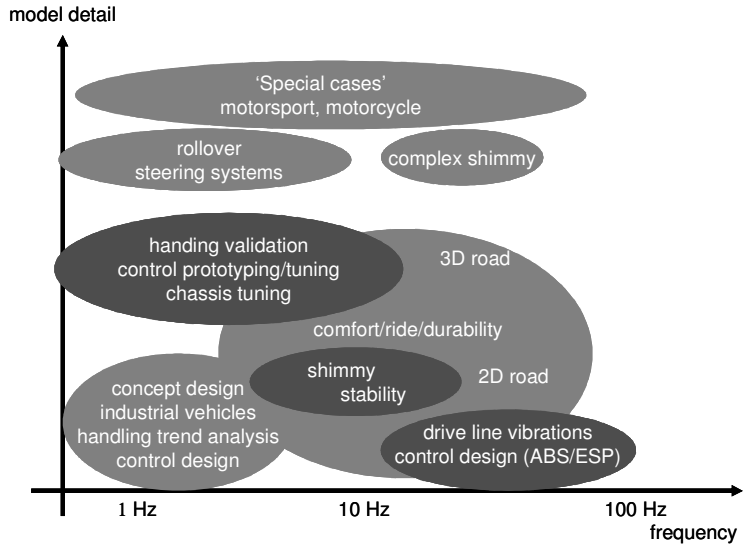

Figure 47.: Main application areas for each tyre model data (from [19])

The situation of a 2D-road (in-plane) with unevenesses of arbitrary shape is important for the assessment of comfort, ride and durability. Dynamic in-plane behaviour of tyres has been tested extensively by hitting a cleat of certain shape. Such a cleat may be a trapezoidal one. The dynamic response of a tyre hitting a trapezoidal cleat with height of 10 mm is shown in figure 48. Both the time histories for vertical and longitudinal force, and the frequency contents of these signals (auto spectral density) are shown. One observes resonances at 80 – 90 Hz and 40 Hz. The first resonance corresponds to a mix of vertical and out of phase circumferential vibration, the second resonance is related to the in phase circumferential vibration.

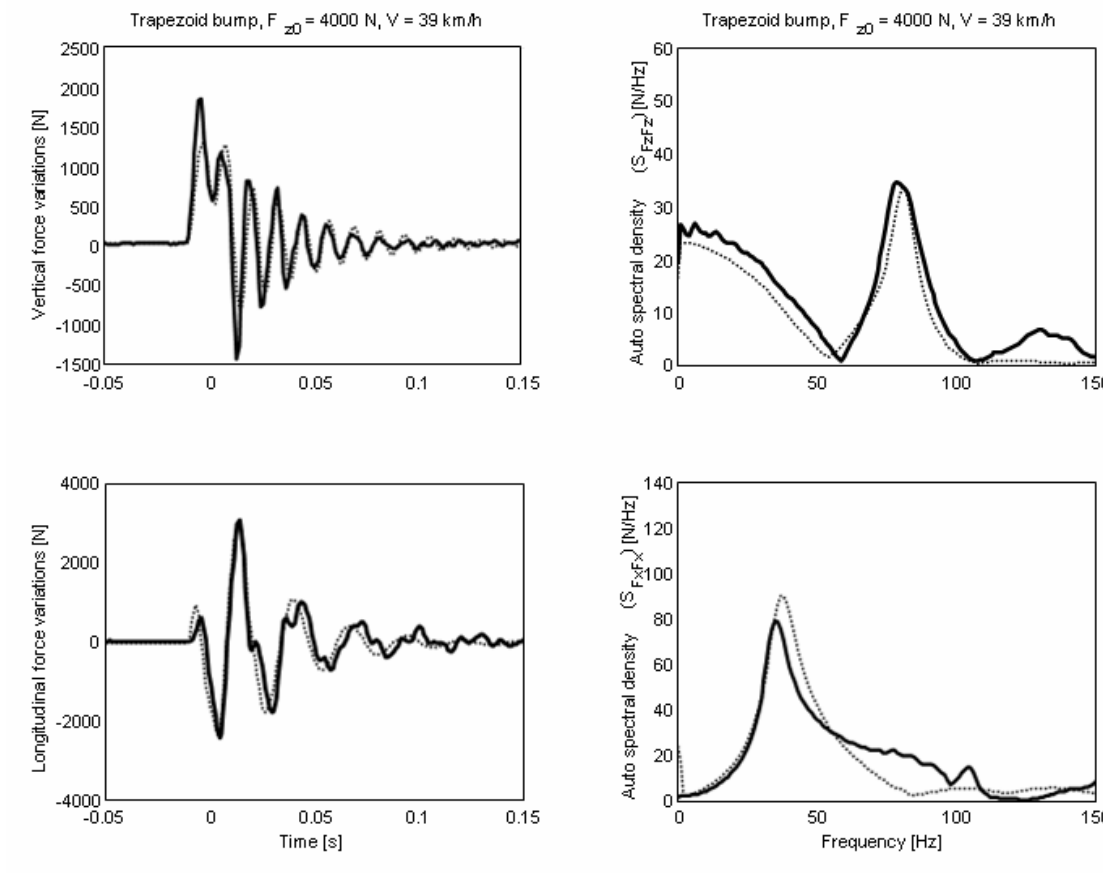

Figure 48.: In-plane dynamic tyre response (from [32])

6.2. Tyre enveloping properties,

We conclude that, in order to model dynamic tyre behaviour up to about 100 Hz, a rigid ring model for the belt is sufficient to include the relevant belt dynamics. On the other hand, a tyre has enveloping properties such that the load impact at the wheel axle for short wavelength road unevenesses can't be described by a rigid belt only, and these properties need to be accounted for. In general, there are two alternative ways to describe dynamic tyre performance:

1. with a rigid belt model, but including some filter model to account for the tyre enveloping properties
2. with a full flexible belt model

The first alternative has the advantage of being efficient with respect to the modelcomplexity. The second option has the advantage of not requiring a separate enveloping model at the cost of a relative large number of degrees of freedom. Examples of this second option are FTIRE (see [12] and [13], and RMODK (see [21]).

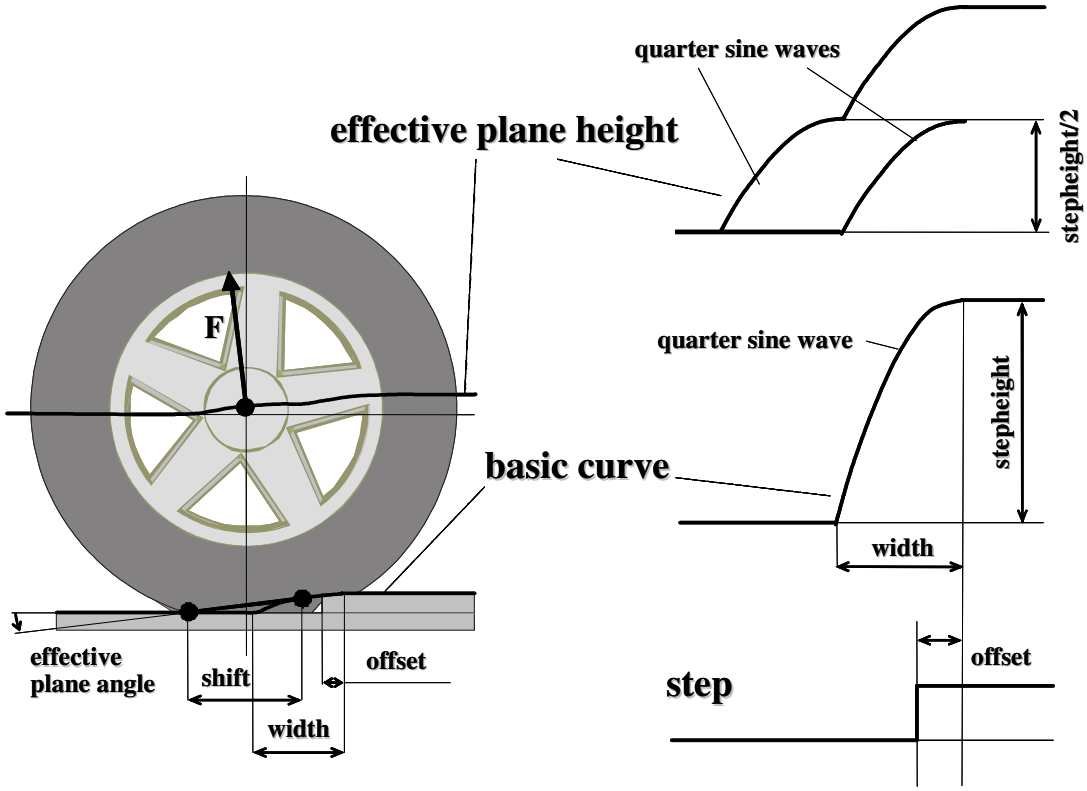

Figure 49.: Enveloping properties tyre

There are different ways to describe the geometric filter. The idea behind it is that a rigid belt model passing some effective road irregularity profile leads to the same quasi-stationary response at the wheel axle as a real tyre passing the real road profile.
Let us consider the situation of a single step. The vertical position of the axle (the effective plane height) for fixed wheel load is depicted in fig. 49.

This **effective plane height** looks like a combination of two quarter sine waves, each with a height equal to the half step height. This behaviour of the wheel axle position can be obtained by pushing a two-point follower system along a single quarter sine wave with height equal to the full step height. The centre point of this system will show the two sine wave behaviour, and the slope of the two-point follower appears to suit well as an effective plane angle, as 'seen' by the tyre as a result of its enveloping properties. This two-point follower has a length of about 80 % of the tyre contact length, and is therefore described in [35] as the 'contact patch'. This second single quarter sine wave is called the **basic function** resulting from the specific road profile (an upward step in this case). Such a basis function can be obtained for any road shape. Think of this as starting from a road profile as a superposition of single road steps. Not all of these steps are 'seen' by the tyre, but this problem can be accounted for.
As observed by Zegelaar, the basic function (for a step change) primarily depends on the step height and not on the tyre load. On the other hand, the two-point follower length (the 'shift' in figure 49) does not depend on the road unevenesses but is

primarily related to the tyre load. As a result, one may use a dynamic tyre model, based on a rigid ring, where the road profile is replaced by the corresponding basic road profile, and where the shift is continuously adjusted to the changing tyre load. Such a model was developed at the Delft University of Technology, now well known under the name SWIFT (Short Wavelength Intermediate Frequency Tyre model), with links to many standard vehicle dynamics simulation tools such as ADAMS, SIMPACK, MADYMO (see for example references [1] and [19]).

Schmeitz [32] improved the enveloping model by introducing the tandem model with elliptical cams, shown in figure 50. The tandem base length corresponds 80 % of the contact length Both elliptical cams follow the road profile. As a result, the effective plane heigth follows from the height of the midpoint of the tandem rod. Note that the cams are only allowed to move in vertical direction (vertical sliders).
It was shown in [32] that the shape of the elliptical cams is affected by neither the vertical load, nor the step height (in case of a step change).

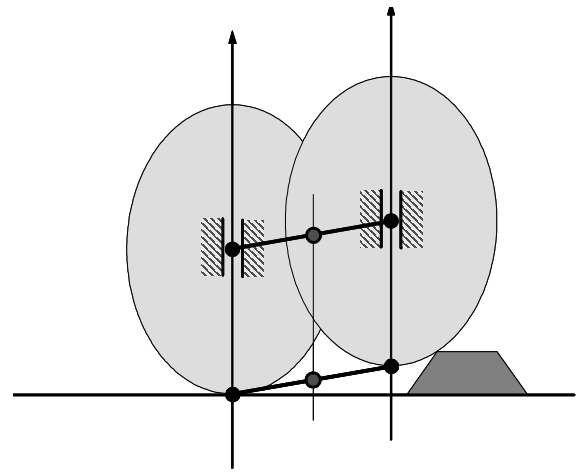

Figure 50.: Tandem model with elliptical

6.3. The rigid ring tyre model

The concept of elliptical cams has further been extended to multi-track systems with a finite number of parallel tandems. In that way, oblique step inputs can be dealt with, or

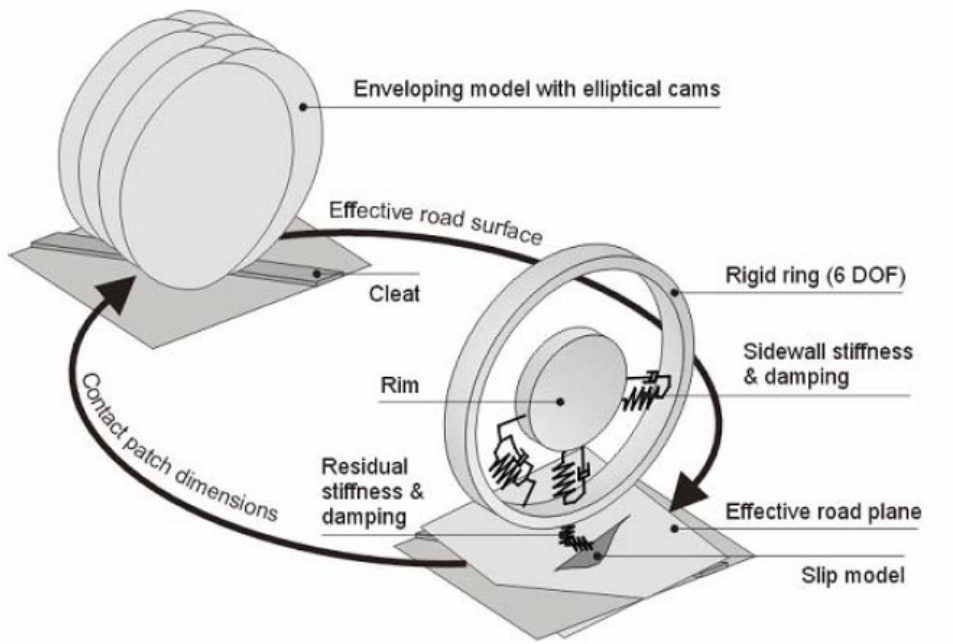

Figure 51.: Full SWIFT rigid ring tyre model

longitudinal step inputs with a nonzero slip angle. We refer to figure 51 for the full SWIFT rigid ring tyre model. As discussed before, the tyre tread band is modelled as a rigid ring, i.e. a circular rigid body, suspended to the wheel rim through stiffnesses in radial and circumferential direction (in-plane) and in yaw, camber and lateral direction (out-of-plane). The rigid ring is linked to the ground through a contact model, usually based on transient and steady state magic formula descriptions. The residual stiffness is used to ensure that the overall quasi-static tyre stiffness is modelled correctly.

7. Experimental assessment of tyre characteristics

Tyre characterisytics are assessed, either on the road or in the laboratory. Tests on the road are realistic, but in general not reproducible. Tests in the laboratory on a drum with diameter in the order of 2 – 2.5 m are reproducible but not realistic regarding the surface conditions. Other possibilities in a laboratory are the inside of a drum (allowing in-door tests for a wet road) or a belt machine. The latter one has a steel belt, kept flat by hydrostatic bearings.

An important problem is the temperature in combination with the fact that the slip conditions during tests to derive tyre characteristic data are, in general, not realistic. A sweep in slip angle between -5 and + 15 ^{O} within some seconds leads to high temperatures, affecting these characteristics. Combined slip conditions, i.e. a fixed slip angle under braking torque may lead to erroneous tyre characteristics for the same reason.

For an important parameters such as the cornering stiffness, a difference of 30 % has been observed. For the aligning torque, this variation may be even much larger. Carrying out measurements under conditions, comparable with the realistic driving circumstances, these differences can be brought back to the deviations that can be attributed to the change in road curvature. For a 2 m drum, this means an error of about 16 % reducing to about 13 % for a 2.5 m drum.

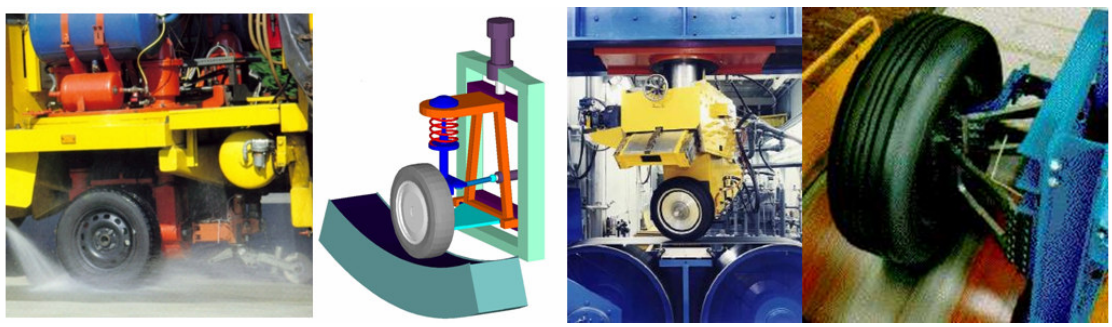

Figure 52.: Some experimental tyre facilities

References.

[1]. ADAMS/tire User Guide. Part 120TIRG-01. Mechanical Dynamics Inc. (2002).

[2]. D.J. Bickerstaff.: *The Handling Properties of Light Trucks*. SAE 760710

[3]. F. Böhm.: *Der Rollvorgang des Automobil-Rades*, ZAMM 43, T56 – T60 (1963).

[4]. W. Borgmann.: *Theoretische und Experimentelle Untersuchungen an Luftreifen bei Schräglauf,* Diss., Braunschweig (1963).

[5]. J.C. Dixon .: *Tyres, Suspension and Handling*, Cambridge University Press, Cambridge, 1991.

[6]. E. Fiala.: *Seitenkräfte am rollenden Luftreifen,* VDI Zeitschrift 96, 973 (1964)

[7]. F. Frank.: *Grundlagen zur Berechnung der Seitenführungskennlinien von Reifen*, Kaut. Gummi 8 (18), 515 (1965).

[8]. F. Frank (2).: *Theorie des Reifenschräglaufs*, Diss. T.H. Darmstadt (1965).

[9]. G. Freudenstein.: *Luftreifen bei Schräg- and Kurvenlauf*, Deutsche Kraftf. Forsch. and Str.Verk.Techn., Heft 152 (1961)

[10]. G. Genta.: *Motor Vehicle Dynamics, Series on Advances in Mathematics for Aplied Sciences* Vol 43. World Scientific (1997).

[11]. M. Gerresheim, A. Hussmann.: *Kräfte und Bewegungen in der Aufstandsfläche geradeausrollender Reifen, Teil 1*. Automobil-Industrie 3/75.

[12]. M. Gipser.: *FTire, a New Fast Tire Model for Ride Comfort Simulations*. ADAMS User Conference Berlin {1999)

[13]. M. Gipser, R. Hofer, P. Lugner.: *Dynamical Tire Forces Response to Road Unevenesses*. In.: Tyre Models for Vehicle Dynamic Analysis. Supplement to Vehicle System Dynamics, Vol. 27, Swets & Zeitlinger (1997)

[14]. R. Gnadler.: *Nassgriff und Aquaplaningverhalten von PKW-Reifen, Verkehrsunfall und Fahrzeugtechnik* (1988)

[15]. E. Hadekel.: *The mechanical characteristics of pneumatic tires*, S&T Memo No 10/52 (British Ministry of Supply, TPA 3/TIB, 1952).

[16]. Higuchi.: *Transient Response of TYres at Large Wheel Slip and Camber*. Thesis Delft University of Technology, 1997.

[17]. J R.M.M. Hogt.: *The prediction of brake deceleration from road roughness tests* (in Dutch). TNO-Report 740710375 (1998).

[18]. .P. Maurice.: *Short Wavelength and Dynamic Tyre Behaviour under Lateral and Combined Slip Conditions.* Ph.D Thesis, Delft University of Technology, The Netherlands (1999).

[19]. MF-Tyre & MF-Swift 6.0, User Manual. TNO-publication www.delft-tyre.com

[20]. D.F. Moore.: *The Friction of Pneumatic Tyres.* Elsevier Scientific Publishing Company (1975).

[21]. Ch. Oertel, A. Fandre.: *Ride Comfort Simulations and Steps Towards Life Time Calculations: RMOD-K and ADAMS,* ADAMS User Conference, November 17-19 (1999)

[22]. H.B. Pacejka.: *The Tyre as a Vehicle Component*. XXVI FISITA Congress, Prague, June 16 – 23 (1996)

[23]. H.B. Pacejka (2).: *Tyre and Vehicle Dynamics*. Butterworth-Heinemann. (2002)

[24]. H.B. Pacejka (3).: *The wheel shimmy phenomenon*, Diss., Techn. University of Delft (1966)

[25]. H.B. Pacejka (6).: *The tyre as a vehicle component, yaw and camber analysis*, Chap. 7.5 of Mechanics of Pneumatic Tyres, ed. S.K. Clark, pp. 757 – 839, N.B.S. Monograph 122, Washington D.C. (1971) (New edition 1981).

[26]. H.B. Pacejka (4).: *Some recent investigations into dynamics and frictional behaviour of pneumatic tyres,* The Physics of Tyre Traction, eds. D.F. Hays and A.L. Browne, Proc. of symposium held at Gen. Motors Res. Lab. (Mich. 1973), Plenum Press, New York (1974).

[27]. H.B. Pacejka (5) and P.S. Fancher.: *Hybrid simulation of shear force development of a tyre experiencing longitudinal and lateral slip*, Proc. XIV Int. Auto, Tech. congress FISITA, London, June 1972, p. 3/78.

[28]. W. Pasterkamp.: Ph-D thesis, Delft University of Technology

[29]. J.P. Pauwelussen, A.L.A. Andress Fernandez.: *Estimated combined steady state tyre slip characteristics,* Haus der Technik Conference 2001: Fahrwerktechnik, Osnabrück, Germany

[30]. J.P. Pauwelussen.: *The Local Contact Between Tyre and Road Under Steady State Combined Slip Conditions*. J. Veh. System Dynamics, Vol 41, no. 1 (2004)

[31]. Savkoor, A.R.: *The lateral flexibility of pneumatic tires and its application to the lateral rolling contact problem*, SAE paper 700378, FISITA/SAE congress (1970)

[32]. A.J.C. Schmeitz.: *A Semi-Empirical Three-Dimensional Model of the Pneumatic Tyre Rolling over Arbitrarily Uneven Road Surfaces.* Ph.D Thesis, Delft University of Technology, The Netherlands (2004).

[33]. *Textuur*, KOAC-NPC note (in Dutch), http://www.koac-npc.nl/webbits/site/NL/Page.asp?PageID=4058

[34]. *Truck tyre basics.* Continental publication 01311107

[35]. P.W.A. Zegelaar.: *The Dynamic Response of Tyre to Brake Torque Variations and Road Unevenesses.* Ph.D Thesis, Delft University of Technology, The Netherlands (1998).

[36]. http://media.bonnint.net/wgms/0/77/7736.gif

[37]. http://www.autotrain-europe.com/resources/aachen/Automotive_Engineering_II/Script_PDF/chapter3.pdf